

**SIMULATION OF FLUID FLOW WITH TEMPERATURE
GRADIENTS IN KARST RESERVOIRS**

BY

AbdAllah AbdRabElNaby Youssef ElSaiced

A Thesis Presented to the
DEANSHIP OF GRADUATE STUDIES

KING FAHD UNIVERSITY OF PETROLEUM & MINERALS

DHAHRAN, SAUDI ARABIA

1963 ١٣٨٣

In Partial Fulfillment of the
Requirements for the Degree of

MASTER OF SCIENCE

In

PETROLEUM ENGINEERING

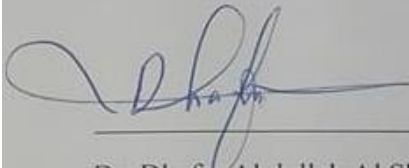
January 2018

KING FAHD UNIVERSITY OF PETROLEUM & MINERALS

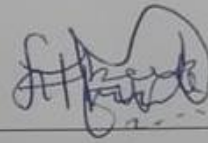
DHAHRAN- 31261, SAUDI ARABIA

DEANSHIP OF GRADUATE STUDIES

This thesis, written by **AbdAllah AbdRabEINaby Youssef** under the direction his thesis advisor and approved by his thesis committee, has been presented and accepted by the Dean of Graduate Studies, in partial fulfillment of the requirements for the degree of **MASTER OF SCIENCE IN PETROLEUM ENGINEERING.**



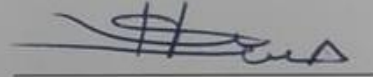
Dr. Dhafer Abdullah Al Shehri
Department Chairman



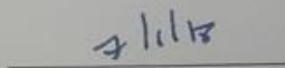
Dr. Abeebe Abewole Awotunde
(Advisor)



Dr. Salam A. Zummo
Dean of Graduate Studies



Dr. Hasan Yousef Ali Al-Yousef
(Member)



Date



Dr. Shirish Patil
(Member)

© AbdAllah AbdRaabElNaby Youssef

2018

[Dedication

To those who pushed me all the way from the start to the end of the road,

to my parents, my wife, my son, my brother and my sisters;

AbdRabElNaby and Azza

Salma

Aser

Mohamed

Esraa, Salma and Baraah]

ACKNOWLEDGMENTS

Looking back to this thesis work, I realize that my contribution is a small portion of the total efforts done in this work. This thesis work wouldn't have been done without the valuable inputs of several individuals who I would like to thank here.

To my thesis advisor; Dr. Abee Awotunde,

From our very first meeting, you were my fountainhead of motivation and perseverance. Somehow, no matter what difficulties we are facing, I found in our meetings the inspiration to carry on with this research work. I can easily say that without your moral support, other than the technical support, this work wouldn't have been done the way it is presented here today.

To my committee members;

Dr. Hasan Al-Yousef

Thank you for introducing me to the world of reservoir simulation and for your beneficial comments.

Dr. Shirish Patil

Thank you for being a part of this committee.

|

TABLE OF CONTENTS

ACKNOWLEDGMENTS	V
TABLE OF CONTENTS	VI
LIST OF TABLES	IX
LIST OF FIGURES	X
LIST OF ABBREVIATIONS	XIII
ABSTRACT	XIV
ملخص الرسالة	XVI
CHAPTER 1 INTRODUCTION	1
1.1. Motivation and State of Research	1
1.2. Goals of the Thesis	4
CHAPTER 2 LITERATURE REVIEW	6
2.1. Karst Reservoirs and Aquifers	6
2.1.1. Introduction	6
2.1.2. Karstification Process	6
2.1.3. Karst Porosity	7
2.1.4. Karst Caves	7

2.2.	Mathematical Models of Karstic Media	9
2.2.1.	Conservation of Mass	9
2.2.2.	Conservation of Momentum	10
2.2.3.	Conservation of Energy	15
 CHAPTER 3 METHODOLOGY.....		16
3.1.	Finite-Volume Discretization	16
3.1.1.	Discretization of Conservation Equation of Mass	16
3.1.2.	Discretization of Conservation Equation of Momentum	18
3.1.3.	Discretization of Conservation Equation of Energy.....	19
3.2.	Solution	20
3.3.	Darcy Model with Estimated Permeability Distribution (DMEPD).....	22
3.3.1.	Analytical solution	23
3.3.2.	Flow in Caves Not Aligned with the Principal Direction of Flow	28
 CHAPTER 4 RESULTS, DISCUSSION AND CONCLUSION.....		33
4.1.	Application Examples of Thermal Flow Simulation in Karstic Media	33
4.1.1.	Example 1 (Simple Model)	33
4.1.2.	Example 2	37
4.2.	Sample Applications of DMEPD	40
4.2.1.	Example 1: Channel Flow	40
4.2.2.	Example 2: Underground River	41
4.2.3.	Example 3: Advection-dominant flow in karst reservoir	48
4.2.4.	Example 4: Tilted Channel	50

4.3. Conclusion.....	52
REFERENCES.....	57
APPENDIX : ANALYTICAL SOLUTION OF STOKES-BRINKMAN'S EQUATION.....	62
VITAE.....	66

LIST OF TABLES

Table 1 Classification of Carbonate Pores, Cavities, and Fractures [38].	8
Table 2 Simple model parameters.....	34

LIST OF FIGURES

Figure 1 Actual velocity profile of coupled flow.....	3
Figure 2 Connections of adjacent grids to Grid Block m. Rates q_x and q_y are computed at grid interfaces while pressures are computed at grid centers.....	17
Figure 3 Flow chart of solution steps.....	22
Figure 4 Apparent velocity distribution for a channel surrounded by porous media on each side.....	25
Figure 5 Variation of apparent channel permeability with respect to Darcy permeability at different ratios of porous media permeability with respect to channel Darcy permeability.	26
Figure 6 Effect of $\frac{\mu}{\mu^*}$ on the calculated apparent permeability.....	27
Figure 7 Flow chart of DMEPD.....	29
Figure 8 Flow chart of DMWEPD.....	30
Figure 9 Flux continuity across interface between two grid blocks.	32
Figure 10 (a) Simple caved aquifer model (b) Magnification of the region surrounded by brown box	35
Figure 11 Temperature distribution in $^{\circ}R$ at 100days using Stokes-Brinkman’s model (Hint: - the sizes of all the grid blocks are equal for the sake of visualization)	36
Figure 12 Temperature distribution in $^{\circ}R$ at 100days using Darcy model (Hint: - the sizes of all the grid blocks are equal for the sake of visualization)	37
Figure 13 Temperature of the fluid produced from production well	37

Figure 14 Temperature distribution in $^{\circ}R$ at 100days using Brinkman’s equation and grid width 0.5 ft. in y-direction around interface between porous media and free-flow region (Hint: - the sizes of all the grid blocks are equal for the sake of visualization)	38
Figure 15 Effect of grid cells size around interface between porous media and free-flow region on the produced fluid temperature.....	38
Figure 16 Permeability distribution in md of complicated caved aquifer model (Hint: - the cave is in yellow)	39
Figure 17 Produced fluid temperature from production wells (complicated model).....	40
Figure 18 Estimated permeability (md) distribution calculated from analytical solution for DMEPD of the channel flow case.....	41
Figure 19 Velocity profile for channel case using different approaches.	42
Figure 20 Variation of $\frac{t_{S-B}}{t_{DMEPD}}$ with model number of grids.	42
Figure 21 Estimated permeability distribution (md) of underground river case	43
Figure 22 Velocity profile for underground river case using different approaches.....	43
Figure 23 Velocity profile using Stokes-Brinkman at different grid width.....	45
Figure 24 Velocity profile near the interfaces and boundaries using Stokes-Brinkman at different grid width.	46
Figure 25 Ratio of max anticipated velocity using numerical Stokes-Brinkman to max Poiseuille’s velocity using actual area of free flow region and apparent area (start from center of first grid inside porous media adjacent to interface) at various grid widths.....	46
Figure 26 Velocity profile using DMEPD at different grid width.....	47

Figure 27 Velocity profile near the interfaces and boundaries using DMEPD at different grid width.	47
Figure 28 Temperature distribution in $^{\circ}R$ using different approaches at 200day for constant viscosity fluid (Hint: - the sizes of all the grid blocks are equal for the sake of visualization)	49
Figure 29 Produced fluid temperature (slight change in viscosity)	49
Figure 30 Temperature distribution in $^{\circ}R$ using different approaches at 200day for strong variable viscosity fluid (Hint: - the sizes of all the grid blocks are equal for the sake of visualization).....	50
Figure 31 Produced fluid temperature (sharp change in viscosity)	50
Figure 32 Permeability distribution (mD) and inclination angle (θ) of tilted channel case.....	51
Figure 33 Pressure contour maps (colored maps) and streamline profile (blue) diagram with velocity profile (red) using both DMEPD (left) and Stokes-Brinkman (right) for different inclination angles.....	55
Figure 34 Surface pressure distribution for $\theta = \pi/2.838$ using DMEPD (left) and Stokes-Brinkman (right).	56
Figure 35 Pressure distribution (psi) using DMWEPD without using GCP.....	56

LIST OF ABBREVIATIONS

BJS	:	Beavers, Joseph and Saffman
DMEPD	:	Darcy Model with Estimated Permeability Distribution
GCP	:	Globally-Coupled pressure Method

ABSTRACT

Full Name : AbdAllah AbdRabElNaby Youssef ElSaieed

Thesis Title : Uncertainty Propagation and Simulation of Fluid Flow with
Temperature Gradients in Karst Reservoirs

Major Field : Petroleum Engineering

Date of Degree : [January 2018]

The simulation of fluid flow in fractured-vuggy reservoirs is a challenging task. The presence of free-flow media (fractures, vugs, and caves) at multiple scales introduces non-Darcian flow regimes and significantly affects the flow paths in the reservoir. The presence of these different complexities in a karst reservoir necessitates the use of non-traditional reservoir modelling techniques. Assigning high permeability to the free-flow regions is considered to be a suitable approach in the case of single-phase, isothermal flow. However, using this approach leads to inaccurate model response in the case of non-isothermal flow in karst reservoirs.

The first point that is tackled in this study is the simulation of a single-phase, non-isothermal flow within karst reservoirs containing macro features such as caves. Two synthetic karst reservoir models are used for this study. The Stokes-Brinkman's equation is used to couple the flow mechanics in the porous media to the flow in the free-flow media. The temperature distribution in the proposed reservoir is modeled. The conservation of

mass and Stokes-Brinkman's equations were solved simultaneously for pressure and flow rate. The energy equation was then solved sequentially for the temperature distribution in the reservoir. The results are then compared with a control case that simplifies the free-flow regions as extremely high permeable region and is modelled using Darcy's equation.

The computational costs associated with the use of Stokes-Brinkman (or single domain approach) is much higher when compared with the use of Darcy model while Darcy-Stokes (known as double domain approach) requires the implementation of the interface conditions. The second target of this research is introducing an approximation technique that assigns different permeability values to the grids in the free-flow region. The technique computes (apparent) permeability values (for different grid locations in the free-flow regions) that make it possible for the Darcy model to closely approximate the Stokes-Brinkman's model. This makes it possible to replace the Stokes-Brinkman model with the Darcy model without significant loss of accuracy in modelling flood fronts. The values of the apparent permeability of the grids inside the free-flow region and the surrounding porous media are calculated from the analytical solution of Stokes-Brinkman's equation. Four examples using synthetic reservoir models are presented to illustrate the effectiveness of this technique. In the first three examples, the principal axes of the cave (free-flow region) align with those of the porous media. The fourth example consists of a more complex scenario in which the principal axes of the cave are not in alignment with those of the porous media.

ملخص الرسالة

الاسم الكامل: عبدالله عبدرب النبي يوسف السعيد

عنوان الرسالة: محاكاة تدفق السوائل في الخزانات الكارستية مع انحدار درجات الحرارة

التخصص: هندسة البترول

تاريخ الدرجة العلمية: يناير 2018

إن محاكاة تدفق السوائل في الخزانات المتشققة و المجوفه هي مهمة صعبة. وجود مناطق التدفق الحر (الكسور، والفجوات، والكهوف) على مستويات متعددة يقدم أنظمة تدفق غير دارسية ويؤثر بشكل كبير على مسارات التدفق في الخزان. وجود هذه التعقيدات المختلفة في خزان الكارست يستلزم استخدام تقنيات النمذجة غير تقليدية للخزان. ويعتبر تعيين نفاذية عالية لمناطق التدفق الحر نهجا مناسباً في حالة وجود مائع واحد و تدفق متساوي الحرارة. ولكن فإن استخدام هذا النهج يؤدي إلى نموذج غير دقيقة في حالة تدفق غير متساوي الحرارة في الخزانات الكارستية.

النقطة الأولى التي تم تناولها في هذه الدراسة هي محاكاة تدفق سائل أحادي الطور غير متساوي الحرارة داخل خزانات الكارست يحتوي على سمات ضخمة مثل الكهوف. تم استخدام اثنين من نماذج الخزانات الكارستية المفترضه لهذه الدراسة. يتم استخدام معادلة ستوكس-برينكمان لربط آليات التدفق في النسيج الصخري و مناطق التدفق الحر. يتم محاكاة توزيع درجة الحرارة في الخزانات المقترحة. يتم حل معادلة بقاء الكتله و معادله ستوكس-برينكمان في وقت واحد للحصول علي الضغط ومعدل التدفق. ثم يتم حل معادلة بقاء الطاقة بالتتابع للحصول علي لتوزيع درجة الحرارة في الخزان. ثم تتم مقارنة النتائج مع حالة تبسيط مناطق التدفق الحر كمنطقة نفاذية عالية للغاية باستخدام معادلة دارسي.

الوقت المستهلك لاجراء العمليات الحسابية المرتبطة باستخدام ستوكس-برينكمان هي أعلى بكثير بالمقارنة مع استخدام نموذج دارسي في حين أن دارسي-ستوكس يتطلب وجود شروط السطح الفاصل بين النسيج الصخري و المناطق حرة التدفق. الهدف الثاني من هذا البحث هو إدخال تقنية تقريبية تقوم علي تعيين قيم نفاذية مختلفة للخلايا في منطقة التدفق الحر. وتحسب هذه التقنية قيم النفاذية الظاهرية (لمواقع الخلايا المختلفة في مناطق التدفق الحر) التي تجعل من الممكن لنموذج دارسي أن يقترب بشكل جيد من نموذج ستوكس برينكمان. وهذا يجعل من الممكن استبدال نموذج ستوكس برينكمان مع نموذج دارسي دون فقد كبير من الدقة في نمذجة جبهات الاغراق. يتم حساب قيم النفاذية الظاهرة للخلايا داخل منطقة التدفق الحر والنسيج الصخري المسامي المحيط من الحل التحليلي لمعادلة ستوكس برينكمان. يتم عرض أربعة أمثلة لنماذج خزانات مفترضة لتوضيح فعالية هذه التقنية. في الأمثلة الثلاثة الأولى، المحاور الرئيسية للكهف (منطقة التدفق الحر) تتماشى مع محاور النسيج الصخري و النموذج. المثال الرابع يتكون من سيناريو أكثر تعقيدا حيث المحاور الرئيسية للكهف ليست في موازاة مع تلك الخاصة بالنسيج الصخري. |

CHAPTER 1

INTRODUCTION

1.1. Motivation and State of Research

The numerical modelling of carbonate karst aquifers is considered to be one of the more challenging and attractable problems to be studied. Many water aquifers are related to paleokarst, such as Yarqon-Taninim aquifer [1], Buda thermal karst system [2] and Guang'an Longtan reservoir [3].

Karstification is a geological process that produces morphological features of the karst topography including caverns and channels. Karst reservoirs are separated into two types: 1) microkarst, 2) megakarst. Microkarsts are defined as consisting of vugs and fractures having openings so small that they cannot be observed by routine borehole logging tools but can only be observed through the cores and from nuclear magnetic resonance and borehole imaging tools. Megakarsts on other hand is a term used to define karst reservoirs consisting of large conduits and caves [4]. Underground caves are openings that are in some cases large enough to accommodate humans [5]. Underground caves often provide natural access to oil and groundwater and also act as access ways for exploratory or drilled openings. These karstic caves are the main source of heat for many wells and springs that are used to generate energy. Primary examples of these features are the baths of Budapest, Hungary [6,7] and the thermal springs in Stuttgart, Germany [8].

Acidic water that contains the CO_2 can dissolve the carbonate rock due to a set of chemical reactions that can be simplified as: -



It was reported that temperature is an important factor in the formation of karsts and that low temperatures favor karstification process [9,10]. The experiments conducted in [4] demonstrated that one liter of water at 0°C dissolved 4–5 times more limestone than water at 30°C and 6 times more than water at 40°C.

Modeling flow through such heterogeneous reservoirs and aquifers with coexistence of free-flow and porous regions is considered a complex problem [11,12]. The transport equation to model flow in a free-flow region is the Navier-Stokes equation while the required equation in the porous media is Darcy's equation. The effect of viscous shear in the unobstructed channel flow parallel to the surface of a porous media is experimentally proven to penetrate the permeable surface to form a boundary layer in the porous medium as shown in Figure 1 [13,14]. The two approaches proposed to couple the two different flow behaviors are: -

1. Double domain approach (Coupled Darcy-Stokes approach).
2. Single domain approach (Stokes-Brinkman's equation).

Double domain approach uses Navier-Stokes equation to model the transport of fluids in the free-flow region and Darcy's equation to model the transport of fluids in the porous region. However, Darcy's law is not compatible with the existence of a boundary layer region in the porous medium because no macroscopic shear term (second order term) is present in Darcy's law [15]. To model this change in velocity at the boundary, Beavers, Joseph and Saffman proposed the BJS interface boundary condition, a mathematical equation that introduces a fluid slip phenomenon of the tangential velocity component at

the interface between porous media and free-flow region [13]. The jump in the velocity is related to the fine structure of the interface. In addition to this condition, it is essential to conserve both mass and stress normal to the interface [16].

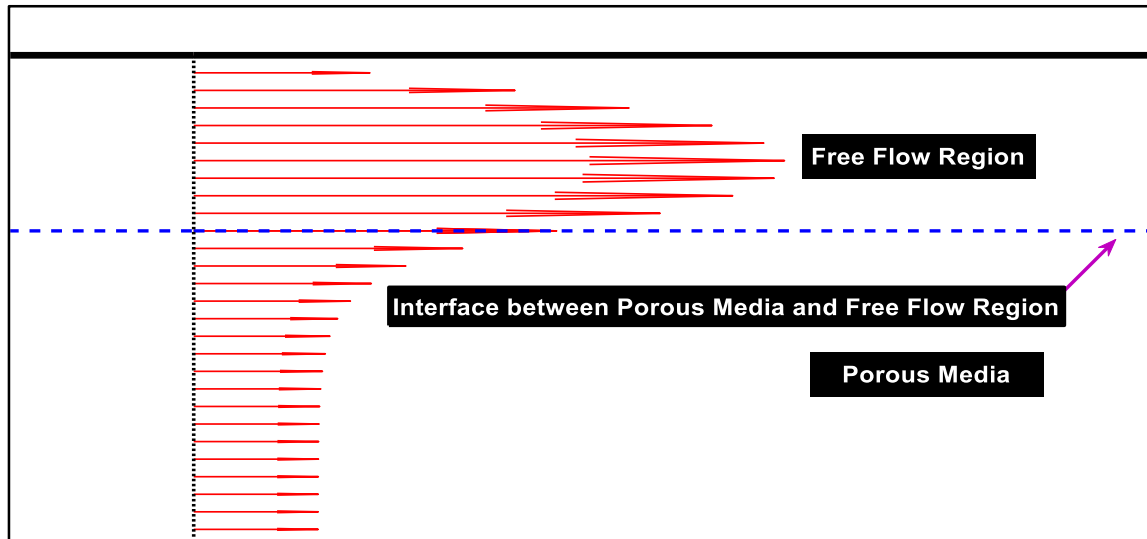


Figure 1 Actual velocity profile of coupled flow

Motivated by the complexity of modeling flow in a coupled free-flow and porous region, Brinkman, 1949, developed a general equation that can be used to model the coupled flow without the need to define additional interface boundary conditions [17]. The Brinkman's equation incorporates the effect of viscous shear in Darcy's model. One of the greatest advantages of using the Brinkman's equation is that it can theoretically switch between the Stokes equation and Darcy's equation (position dependent parameter equation). Brinkman's equation, therefore, offers a more realistic model over the double domain approach [18]. The BJS boundary condition models a slip velocity at the interface between porous media and free-flow region which is not actually what happens. In actual flow, the free-flow velocity gradually decreases inside the porous media until it becomes equal to the Darcy velocity [15]. Majority of studies have been devoted to model single phase

isothermal flow in karstic media using both analytical approaches [15,19] and numerical approaches using finite element [11,18] or using the finite difference instead of the finite element [20,21].

Krotkiewski et al. [22] asserted that, in the case of single-phase, isothermal flow where $k_p < 10^{-4} k_f$, the use of Stokes-Brinkman equation is unnecessary. This is because in such cases, Darcy's law would adequately model the resulting pressure distribution in the free flow region and the porous regions by assigning very high permeability values to the free-flow regions. This implies that single domain or double domain approaches are only important in modeling single-phase isothermal flows in reservoirs with sub-millimeter.

Unfortunately, none of the previously mentioned studies tackled the cases that involve the mega-karst aquifers that have temperature gradient. Also, no simple approach was found in the literature that can be used to simulate fluid flow in simple karstic media without the need to use single domain approach or double domain approach due to difficulties associated with them.

1.2. Goals of the Thesis

Existing literature is replete with studies on isothermal flow of fluids in karst reservoirs (see e.g. [12,18]). To the best of our knowledge, no work has been performed on modeling fluid flow in karst reservoirs under non-isothermal flow using the Stokes-Brinkman's equation. Also, most of the simulation studies that have already been done deals with microscale and mesoscale vugs and fractures such as the modeling of geothermal karst aquifer in Weibei, Shaanxi Province, China [23].

The previous considerations imply that the first target of this study is to model fluid flow with thermal gradients in karst aquifers. This research aims to build the cornerstone of thermal fluid flow simulation in caved aquifers by performing simulation studies of the flow of fluids using the Brinkman's equation on a field scale and concentrate more on large caves. To model the flow of single phase fluid, a finite-volume, implicit pressure, standard volumetric flow rate and temperature are used. At every time-level, the system is solved for pressure and flow rate in the first stage, then solved for temperature in the following step. The same problem is then solved using Darcy's equation in the entire karst aquifer (as a single continuum model) placing very high permeability values in the caves. The results from these two models (Darcy and Stokes-Brinkman) are compared to show the differences in temperature profiles obtained at the production well.

The second target of the research is an alternative approach to model fluid flow in karst reservoirs. This approach, named Darcy Model with Estimated Permeability Distribution (DMEPD), is simple and computationally less expensive than the Stokes-Brinkman model. The approach doesn't use the interface conditions that are implemented in Darcy-Stokes approach. Rather, the approach involves pre-calculating the apparent permeability values in the free-flow region and in the surrounding porous media (where the boundary layer is effective) from the analytical solution of Stokes-Brinkman's equation. Then, using Darcy's law to simulate fluid flow in karst reservoirs. |

| CHAPTER 2 |

| LITERATURE REVIEW

2.1. Karst Reservoirs and Aquifers

2.1.1. Introduction

One of the major topographical features in carbonates is the presence of karsts. Karst represents a topography consisting of complex geological features and specific hydrogeological characteristics which are generally formed in carbonate rock reservoirs and are highly heterogeneous. They are mainly composed of limestone, dolomite, gypsum, halite and conglomerates. Carbonate karsts are highly abundant and its most representative morphological features are karrens, tectonic fractures, dolines, shafts, diagenetic fractures, poljes, caves, vugs, ponors, caverns, estavelles, intermittent springs, lost rivers, stylolite, dry river valleys, intermittently inundated poljes, underground river systems, denuded rocky hills, karst plains and collapses [24].

Many reservoirs and aquifers are related to paleokarst, such as Hainaut carbonate and sulphate karstic aquifer [25], Raspo Mare reservoir [26,27], gas reservoirs of Sinian [28] and Tahe oil reservoir in Tarim Basin in China [29,30]. Between all the cases Tahe oil reservoir is the most popular oil reservoir case due to the presence of large scale and variable distribution karst system.

2.1.2. Karstification Process

Karstification is the process of dissolution of the carbonate rock due to chemical reactions with underground water and mechanical processes. The karstification process may take

millions of years, but small scale caves can form within hundreds to thousands of years [31].

Turbulence plays an important role in determining the effectiveness of the karstification process. It has been experimentally shown that the increase in flow velocity and consequently an increase in turbulence increases the dissolution process, a Reynolds number increase from 250 to 25,000 increased the rate of the dissolution by approximately a factor of 3 [32].

2.1.3. Karst Porosity

The porosity of karst system is defined as the volume of voids of the system of interest relative to total surrounding rock bulk volume [33,34]. Karst porosity can be classified into three component porosity model: -

1. The matrix porosity (pores) that results from sedimentation and diagenesis. This porosity is classified as primary porosity.
2. The fracture porosity (fissures, bedding planes, faults, and joints) that is a result of tectonism, weathering and late diagenesis.
3. The cave porosity (tabular opening or elongated planar) which is a result of speleogenesis. The last two types are considered as secondary porosity [35-37].

2.1.4. Karst Caves

Table 1 reveals the classification of carbonate rock voids [38]. In this work the primary interest is to model the flow in caves. The caves can be defined as the openings that people can access [5]. These karstic caves are the main source of the heat for many wells and

springs that are used to generate energy like the baths of Budapest, Hungary [6,7] and the thermal springs in Stuttgart, Germany [8].

The largest cave system is 560 km long and is called Mammoth cave system in Kentucky, USA. The deepest is the Krubora Cave in Wester Caucasus, Russia and is 2080 deep. The most popular karst oil reservoir is Tahe oil field in China [30]. Buda Karst is considered as the largest thermal water system in Europe out of volcanic areas [2,39].

Table 1 Classification of Carbonate Pores, Cavities, and Fractures [38].

Pore		Cavity		Fracture	
Type	Diameter (mm)	Type	Diameter (mm)	Type	Diameter (mm)
Big pore	50	Huge cavity	>1000	Huge fracture	>100
Mid pore	0.25-0.5	Big cavity	100-1000	Big fracture	10-100
Small pore	0.01-0.25	Mid cavity	20-100	Mid fracture	1-10
Micro pore	<0.01	Small cavity	2-20	Small fracture	0.1-10
				Micro fracture	<0.1

Our work deals with the modelling of flow in karst reservoir on a field scale. Therefore, this work deals with flow through caves and we will neglect the effects of vugs on the much smaller microscale.

2.2. Mathematical Models of Karstic Media

In modelling fluid flow in an aquifer, there is the need to solve a set of coupled differential equations arising from mass balance, momentum balance and energy balance.

2.2.1. Conservation of Mass

The mass balance is often modelled with a continuity equation given by [40]: -

$$-\nabla \cdot (\rho \mathbf{u}) + \dot{q} = \frac{\partial(\phi\rho)}{\partial t} \quad \text{in } \Omega, \quad (2.1)$$

where ρ is the fluid density, \mathbf{u} is the fluid velocity, ϕ is the porosity of the system, t is the time variable, \dot{q} is the mass sink/source term in unit of mass/volume/time and Ω is the domain of interest. Equation (2.1) is used in the entire computational domain but adapted to model flow in both the porous media and the free-flow regions by proper selection and definition of equation parameters as follows: -

- if $\phi = 1$, \mathbf{u} is actual velocity in Ω^f ,

this selection of the porosity and definition of the velocity is appropriate for the free-flow regions.

- if $\phi = \phi_p < 1$, \mathbf{u} is apparent velocity in Ω^p ,

where ϕ_p is the porosity of the porous media. This selection of the porosity and definition of the velocity is appropriate for the porous media.

2.2.2. Conservation of Momentum

To adequately model the flow of fluids through a porous or open media, Equation (2.1) should be coupled with a transport equation. Different models have been proposed in the literature to describe flow in the karst reservoirs. The most well-known three models are Darcy's law, coupled Darcy-Stokes approach and Stokes-Brinkman's equation. The three models are discussed in the subsequent sections.

2.2.2.1. Darcy's Law

The simplest transport model is the Darcy's law given by: -

$$\mathbf{u} = -\frac{1}{\mu} \bar{k} \cdot \nabla p, \quad (2.2)$$

where \bar{k} is the permeability tensor of the medium, μ is the viscosity of the flowing fluid and p is the fluid pressure [41]. Equations (2.1) and (2.2) can be combined together as following: -

$$\nabla \cdot \left(\rho \frac{1}{\mu} \bar{k} \cdot \nabla p \right) + \dot{q} = \frac{\partial(\phi\rho)}{\partial t} \quad \text{in } \Omega. \quad (2.3)$$

Equation (2.3) can be used to model fluid flow in a karst system. However, the use of the Darcy's equation in this case is a simplified approach and may not give accurate models of flood fronts in the free-flow regions of the karst system as it will be shown later in the results. Thus, other approaches involving coupling the more complex Navier-Stokes equation with the continuity equation (Equation (2.1)) is often adopted. The Navier-Stokes equation more accurately models the transport of fluid in the cave while Darcy's equation is appropriate for fluid transport in the porous region. However, the main difficulty arises

in trying to couple the equations representing fluid transport in the different subsystems. Consequently, coupled Darcy-Stokes approach and Brinkman's equation are the two main approaches that are extensively used to model this phenomenon trying to handle the transition of flow from the free-flow region to the porous region (and vice versa).

2.2.2.2. Double Domain Approach (Coupled Darcy-Stokes Model)

Coupled Darcy-Stokes model uses the Navier-Stokes equation to model fluid transport in the free-flow region and the Darcy's equation to model flow in the porous region. Appropriate boundary conditions are used at the interface between the porous region and the free-flow region. Beavers et al. developed a mathematical equation that introduces a fluid-slip phenomenon at the boundary which then was known as BJS (Beavers, Joseph and Saffman) interface boundary condition: -

$$(\mathbf{v} - \mathbf{u}) \cdot \mathbf{i}_x = \frac{\sqrt{k}}{\alpha} \frac{\partial(\mathbf{v} \cdot \mathbf{i}_x)}{\partial y} \quad \text{on } \Gamma, \quad (2.4)$$

where \mathbf{v} is the fluid velocity in the free-flow region, \mathbf{u} is the apparent (superficial) velocity in the porous media, \mathbf{i}_x is a unit vector parallel to the interface (Γ) in two dimensional flow and α is a dimensionless constant which no general estimate is well-known so far [13]. Different studies showed that α depends on the fine structure of the porous media and, hence, it must be considered as adjustable parameter along the interface [42,43]. Moreover, different studies conducted on various flow geometries presented a specific formula of α for each case (see, e.g., [15,44]).

Practical use of the Darcy-Stokes technique requires the need of conservation of mass and normal stress at the interface in addition to the jump in velocity as follows [16]: -

1. Conservation of mass: -

$$\mathbf{v} \cdot \mathbf{i}_y = \mathbf{u} \cdot \mathbf{i}_y \quad \text{on } \Gamma. \quad (2.5)$$

2. Continuity of normal stress: -

$$2\mu \overline{\overline{D}} \cdot \mathbf{i}_y = p_f - p_p \quad \text{on } \Gamma. \quad (2.6)$$

3. BJS interface tangential velocity jump (refer to Equation (2.4)).

In Equations (2.5) and (2.6), \mathbf{i}_y is the unit normal unit vector on the interface (Γ), $\overline{\overline{D}}$ is the strain rate tensor and p_f and p_p are the fluid pressure in the free-flow region and the porous media, respectively [16].

Various researches have been conducted on the use of Darcy-Stokes model to simulate flow in fractured reservoir. Arbogast used the coupled Darcy-Stokes system to homogenize channeled system using mixed finite element simulation study. The study showed that vugs connectivity is the most critical variable in predicting macroscopic permeability. However, without using the concept of the permeability tensor, the research faced some difficulties to upscale the permeability [16]. Darcy-Stokes system has also been coupled with the stream line simulation to predict water breakthrough in Tahe oil field. The results indicate that using simplified model with high permeability in free-flow region would fail to predict the fast breakthrough in caved reservoirs [29].

The computational cost associated with this approach is not much greater than that associated Darcy's model. However, the coupled Darcy-Stokes approach is very sensitive to interface conditions especially in cases where advection is dominant [45]. Also, it has

been shown that the performance of the system is different depending on the selected interface conditions [46].

2.2.2.3. Single Domain Approach (Stokes-Brinkman's Equation)

Brinkman presented a single equation that models the flow inside both porous media and free-flow region without the need to introduce additional interface conditions (Brinkman 1949). Brinkman added the effect of viscous shear in Darcy's model to provide a seamless transition between the porous media and the free-flow region. The Brinkman's equation is given by: -

$$\mu^* \nabla^2 \mathbf{u} = -\nabla p + \mathbf{F}_g + \mu^* (\nabla \cdot \nabla) \mathbf{u} \quad \text{in } \Omega, \quad (2.7)$$

where \mathbf{F}_g is the body force and μ^* is the effective viscosity. The main advantage of Stokes-Brinkman's equation over Darcy-Stokes model is its ability to incorporate the porous media and the free-flow region by proper selection of parameters of Equation (2.7) as following: -

- if $\mu^* = \mu$, $k \rightarrow \infty$, \mathbf{u} is the actual velocity in Ω^f ,

Equation (2.7) reduces to Navier-Stokes equation that is appropriate for the free-flow region.

- if $\mu^* = 0$, $k = k_p \ll \infty$, $\mathbf{u} = \mathbf{v}$ is the apparent velocity in Ω^p ,

the second order shear term is eliminated and Equation (2.7) reduces to Darcy's law.

Durlofsky and Brady mentioned that, in the free-flow regions, the pressure gradient term in Equation (2.7) balances the Laplacian term so that the flow is viscous, although, deeper in the porous media the velocity varies very slowly [47]. Therefore, away from the free-flow region, the pressure gradient balances the apparent velocity similar to Darcy's law. Also, From the analytical solution of Equation (2.7) it is realized that the thickness of the boundary shear layer inside the porous media is of order \sqrt{k} and increases as the thickness of free-flow region increases [15]. Therefore, Equation (2.7) can be used throughout the whole computational domain without the need to define additional boundary conditions at the interface between the porous media and the free-flow region. The presence of the second order shear term in the porous media only introduces small perturbations to the Darcy's law as the shear term has a minor effect compared to the pressure gradient in the porous media [11,15,18,21,22].

Originally, Brinkman assigned $\mu^* = \mu$ [17]. However, this approach does not create any difference between actual and apparent velocity in porous media. Some researchers have claimed that the ratio μ/μ^* should be less than unity [48], [49] and others have mentioned that the ratio should be greater than unity [44], [50]. The value of the effective viscosity relies on the fine structure of the interface between the free-flow region and the porous media specially the porosity and tortuosity [18], [22]. Belhaj et al. [51] used a value of

$$\mu^* = \frac{\mu}{\phi}$$

we fix $\mu^* = \mu$ as this has a negligible effect on the solution. Although Stokes-Brinkman's equation represent a single domain equation without the need for the interface conditions, the computational cost associated with numerical simulation using it is very high [45].

2.2.3. Conservation of Energy

Tackling the energy equation in porous media is challenging. Many simplifications have been introduced to incorporate the whole system in one equation. One of the most important assumptions is the local thermal equilibrium between rock and fluid, where rock matrix and fluid in any particular grid are assumed to have the same temperature. The final form of the energy equation under the assumption of local thermal equilibrium can be written as: -

$$\frac{\partial}{\partial t}(\phi\rho_f\varepsilon_f + (1-\phi)\rho_s\varepsilon_s) + \nabla \cdot (\rho_f \hat{h}_f \mathbf{u}) - \nabla \cdot (\overline{\overline{\Psi}} \cdot \nabla T) = q_t \quad \text{in } \Omega, \quad (2.8)$$

where ε_f is fluid specific internal energy, ε_s is solid specific internal energy, ρ_s is solid density, \hat{h}_f is the specific enthalpy, $\overline{\overline{\Psi}}$ is the thermal conductivity tensor, T is temperature and q_t is the energy sink/source term in unit of heat/volume/time.

By using the same previous approach used in the conservation of mass, Equation (2.8) is adequate for the whole domain. In all the cases that are under consideration in this study, it is assumed that the thermal conductivity is isotropic and the following relations are valid

$$\varepsilon_f = c_{v_f} T, \quad \hat{h}_f = c_{p_f} T, \quad \varepsilon_s = c_s T, \quad \Psi = \Psi_f^\phi \Psi_s^{1-\phi},$$

where c_{v_f} is fluid specific heat at constant volume, c_{p_f} is fluid specific heat at constant pressure, c_s is solid specific heat, Ψ_f is fluid thermal conductivity and Ψ_s is solid thermal conductivity. Further details about this energy balance equation in porous media flow can be found in [40].

CHAPTER 3

Methodology

This chapter considers a detailed explanation of the methodology that we have followed to reach to the results. First, the discretization of conservation equations and procedure of simulation are introduced. Then, Darcy model with estimated permeability distribution that is used as an approximation instead of Stokes-Brinkman is explained in details.

3.1. Finite-Volume Discretization

In this section, the discretization of all the previous conservation equations is presented for two-dimensional flow in Cartesian coordinates. Instead of using velocity as a primary variable, the flow rate is used because the flow rate is more intuitive than velocity, and the solution has a faster convergence than when using velocity [21]. The finite-volume method and implicit scheme are used for discretization. Figure 2 is used to illustrate the cell-centered finite-volume discretization used in this work. The unknown rates q_x^{n+1} and q_y^{n+1} are located at the grid interfaces while the unknown pressures are located at the grid centers. The assumptions used are single-phase laminar flow, slightly-compressible aquifer fluid and rock mass and that the fluid is Newtonian.

3.1.1. Discretization of Conservation Equation of Mass

The conservation of mass in two-dimensional Cartesian coordinates can be stated as: -

$$V_b \frac{\partial \left(\frac{\phi}{B} \right)}{\partial p} \frac{\partial p}{\partial t} + \frac{\partial}{\partial x} \left(\frac{A_x u_x}{B} \right) dx + \frac{\partial}{\partial y} \left(\frac{A_y u_y}{B} \right) dy = q_{sc}^{well}, \quad (3.1)$$

where V_b is the bulk volume, B is the formation volume factor, A is the cross-sectional area and q_{sc}^{well} is the fluid withdrawal or injection rate (at standard conditions) at any well drilled into the aquifer. In Equation (3.1), we can replace $\frac{Au}{B}$ with q , the fluid flux across interfaces. Using the finite-volume method and implicit scheme the discretized form of the equation of conservation of mass can be written as: -

$$\left(\frac{V_b}{\Delta t}\right)_m \left(\frac{\partial}{\partial p} \left(\frac{\phi}{B}\right)\right)_m^n p_m^{n+1} + q_{x_{m,m+1}}^{n+1} - q_{x_{m,m-1}}^{n+1} + q_{y_{m,m+1}}^{n+1} - q_{y_{m,m-1}}^{n+1} = q_{sc_m}^{well,n+1} + \left(\frac{V_b}{\Delta t}\right)_m \left(\frac{\partial}{\partial p} \left(\frac{\phi}{B}\right)\right)_m^n p_m^n \quad (3.2)$$

In Equation (3.2), $q_{x_{m,m+1}}^{n+1}$ is the fluid flux across the interface between adjacent grids m and $m + 1$ in the x -direction while $q_{y_{m,m+1}}^{n+1}$ is the fluid flux across the interface between adjacent grids m and $m + I$ in the y -direction.

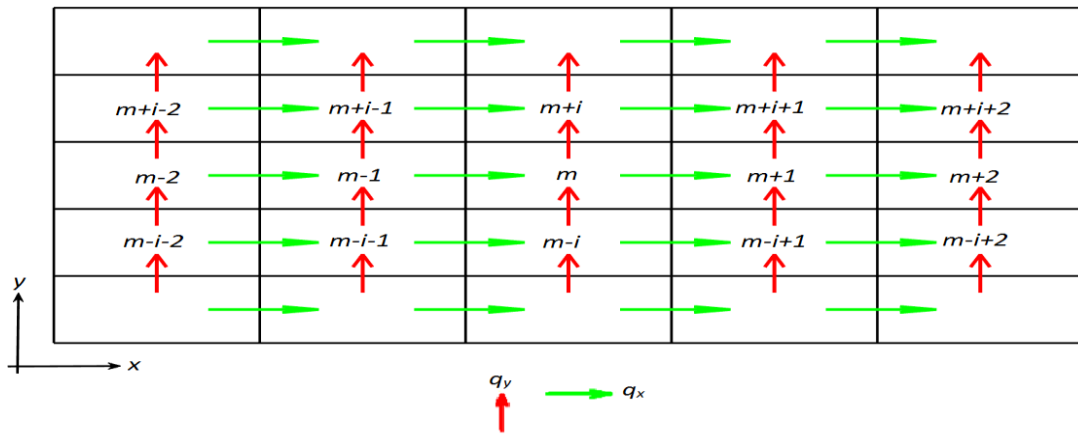


Figure 2 Connections of adjacent grids to Grid Block m . Rates q_x and q_y are computed at grid interfaces while pressures are computed at grid centers.

3.1.2. Discretization of Conservation Equation of Momentum

In the two-dimensional problem, the Stokes-Brinkman's equation has two equations: one in the x -direction and the other in the y -direction. In this subsection, we present the discretization of the Stoke-Brinkman' equation in the x -direction only. The discretization of the equation in the y -direction follows the same steps. The Stokes-Brinkman's equation

in x -direction, when u_x is replaced with $\frac{q_x B}{A}$ is: -

$$\frac{q_x \mu B}{k_x A_x} = - \left(\frac{\partial p}{\partial x} - \frac{\mu B}{A_x} \left(\frac{\partial^2 q_x}{\partial x^2} + \frac{\partial^2 q_x}{\partial y^2} + \frac{\partial^2 q_x}{\partial z^2} \right) \right) \quad (3.3)$$

and by adopting the same approach used in discretizing Equation (3.1), the discretized form of Equation (3.3) is: -

$$p_{m+1}^{n+1} - p_m^{n+1} + \frac{q_{x_{m,m+1}}^{n+1}}{\tau_{m,m+1}^n} - \frac{1}{\zeta_{x_{m,m+1}}^n} \left(\frac{q_{x_{m+1,m+2}}^{n+1} + q_{x_{m,m-1}}^{n+1} - 2q_{x_{m,m+1}}^{n+1}}{\Delta x^2} + \frac{q_{x_{m+1,m+1+1}}^{n+1} + q_{x_{m-1,m-1+1}}^{n+1} - 2q_{x_{m,m+1}}^{n+1}}{\Delta y^2} + \frac{q_{x_{m+11,m+11+1}}^{n+1} + q_{x_{m-11,m-11+1}}^{n+1} - 2q_{x_{m,m+1}}^{n+1}}{\Delta z^2} \right) = 0, \quad (3.4)$$

where $\tau = \frac{k_x A_x}{\mu B \Delta x}$ is the fluid transmissibility and $\zeta = \frac{A_x}{\mu B \Delta x}$.

Harmonic average is used to calculate τ and ζ at the interfaces between grid blocks.

Because we assumed a no-slip boundary condition in z -direction, then we have

$$q_{x_{m+11,m+11+1}} = q_{x_{m-11,m-11+1}} = 0.$$

In this work, the coefficients of q in Equation (3.4) are computed at time-level n (i.e. using the most recent values of pressure and temperature) while q is computed implicitly as shown in the equation. Although this approach reduces the accuracy of the solution, it has the advantage of linearizing the system of equations and reducing the matrix size as will be shown in the following section.

3.1.3. Discretization of Conservation Equation of Energy

The conservation of energy equation in two-dimensional space in Cartesian coordinates can be written as: -

$$\begin{aligned}
V_b \frac{\partial}{\partial t} \left\{ \left[\frac{\phi c_{v_f}}{B} + (1-\phi) \frac{\rho_s c_s}{\rho_{f_{sc}}} \right] T \right\} + \frac{\partial}{\partial x} (q_x c_{p_f} T) dx + \frac{\partial}{\partial y} (q_y c_{p_f} T) dy - \frac{\partial}{\partial x} \left(\frac{\Psi A_x}{\rho_{f_{sc}}} \frac{\partial T}{\partial x} \right) dx \\
- \frac{\partial}{\partial y} \left(\frac{\Psi A_y}{\rho_{f_{sc}}} \frac{\partial T}{\partial y} \right) dy = q_{sc}^{well} c_{p_f} T^{well}.
\end{aligned}
\tag{3.5}$$

By applying the finite-volume discretization, we obtain: -

$$\begin{aligned}
\left(\frac{V_b}{\Delta t} \right)_m \left(\frac{\phi c_{v_f}}{B} + \frac{(1-\phi) \rho_s c_s}{\rho_{f_{sc}}} \right)_m^{n'} T_m^{n+1} + q_{x_{m,m+1}}^{n+1} c_{p_{f_{m,m+1}}}^{n'} T_{m,m+1}^{n+1} - q_{x_{m,m-1}}^{n+1} c_{p_{f_{m,m-1}}}^{n'} T_{m,m-1}^{n+1} + q_{y_{m,m+1}}^{n+1} c_{p_{f_{m,m+1}}}^{n'} T_{m,m+1}^{n+1} \\
- q_{y_{m,m-1}}^{n+1} c_{p_{f_{m,m-1}}}^{n'} T_{m,m-1}^{n+1} - \lambda_{x_{m,m+1}}^{n'} (T_{m+1}^{n+1} - T_m^{n+1}) - \lambda_{x_{m,m-1}}^{n'} (T_{m-1}^{n+1} - T_m^{n+1}) - \lambda_{y_{m,m+1}}^{n'} (T_{m+1}^{n+1} - T_m^{n+1}) - \lambda_{y_{m,m-1}}^{n'} (T_{m-1}^{n+1} - T_m^{n+1}) \\
= q_{sc_m}^{well,n+1} c_{p_{f_m}}^{well,n'} T_m^{well,n+1} + \left(\frac{V_b}{\Delta t} \right)_m \left(\frac{\phi c_{v_f}}{B} + \frac{(1-\phi) \rho_s c_s}{\rho_{f_{sc}}} \right)_m^n T_m^n,
\end{aligned}
\tag{3.6}$$

where $\hat{\lambda}_x = \frac{\Psi A_x}{\rho_{fsc} \Delta x}$ is the thermal conduction transmissibility that is harmonically averaged

at the interfaces between any two grid blocks. The superscript n' means that this parameter is evaluated at old temperature and new pressure. To evaluate the effect of advection on the transport of heat through the media, we used the Peclet number defined as: -

$$P_e = \frac{\text{advection}}{\text{diffusion}} = \frac{\rho_f L u_c c_{p_f}}{\Psi_c}, \quad (3.7)$$

where u_c and Ψ_c are the characteristic velocity and the characteristic thermal conductivity, respectively. It is expected that advection will be more dominant than diffusion in these large caves because the caves can sustain large flow rates and also because the fluid thermal conductivity is much less than rock thermal conductivity. Therefore, the more accurate procedure to obtain the average temperature at grid interfaces is the upwinding technique. For example, the average temperature at the interface between Grid m and Grid $m + 1$ is: -

$$T_{m,m+1} = \begin{cases} T_m & \text{if } q_{x,m,m+1} \geq 0 \text{ (flow from } m \text{ toward } m+1) \\ T_{m+1} & \text{if } q_{x,m,m+1} < 0 \text{ (flow from } m+1 \text{ toward } m) \end{cases}.$$

3.2. Solution

One of the challenges in using Stokes-Brinkman is that there is no way to combine conservation of mass and conservation of momentum in one equation. Instead, we must solve for pressure at the center of the grids and inter-grid rates simultaneously. Therefore, while solving a $N_x \times N_y$ discretized system using the Darcy's model produces only N (where $N = N_x N_y$) unknown pressures, using the Stokes-Brinkman model produces N

unknown pressures in addition to $(N_x - 1)N_y$ unknown rates in x -direction and $(N_y - 1)N_x$ unknown rates in y -direction. This shows that the Stoke-Brinkman model leads to a much larger system of equations than does the Darcy's model for the same problem size. Also, many of the parameters required to compute the coefficients in the Stokes-Brinkman's model are dependent on both pressure and temperature. Thus, to solve the entire problem of fluid flow and heat transport in the karst aquifer with a fully-implicit approach would require the addition of N discrete energy-balance equations to the equations obtained from the Stokes-Brinkman, making the system of equations even bigger and more challenging to solve in a reasonable length of time. Hence, instead of adding N unknown temperatures to the unknown pressures and rates from the discretized flow equations, the coefficients of Equations (3.2) and (3.4) are calculated at previous time-level n . These coefficients are evaluated using old pressures and old temperatures as shown in matrix form: -

$$\begin{bmatrix} M_p^n & M_{q_x} & M_{q_y} \\ \psi_{x_p} & \psi_{x_{q_x}}^n & 0 \\ \psi_{y_p} & 0 & \psi_{y_{q_y}}^n \end{bmatrix} \begin{bmatrix} \vec{p}^{n+1} \\ \vec{q}_x^{n+1} \\ \vec{q}_y^{n+1} \end{bmatrix} = \begin{bmatrix} \vec{R}^n \\ \vec{0} \\ \vec{0} \end{bmatrix} \quad (3.8)$$

In Equation (3.8), the components of the matrix are smaller block-matrices and their elements are evaluated at old time step. M_p^n , M_{q_x} and M_{q_y} are the coefficient block-matrices of pressure, x -direction flow rate and y -direction flow rate, respectively, all generated from the discretization of the mass-conservation equation. ψ_{x_p} and $\psi_{x_{q_x}}^n$ are the coefficient block-matrices of pressure and x -direction flow rate, respectively, both generated from the discretization of the Brinkman's equation in x -direction. Similarly, ψ_{y_p}

and $\psi_{yq_y}^n$ are generated from the discretization of the Stokes-Brinkman equation in the y -direction. Equation (3.8) is then solved for pressures at the center of grid blocks and flow rates at grid interfaces. This newly computed pressure values together with the old temperature values are used to calculate the coefficients of Equation **Error! Reference source not found.** (superscript n'). Finally, the temperatures at the centers of the grid blocks are calculated by solving a system of N linear equations (involving an $N \times N$ matrix) formed from Equation **Error! Reference source not found.** . These steps are summarized in the flow chart shown in Figure 3.

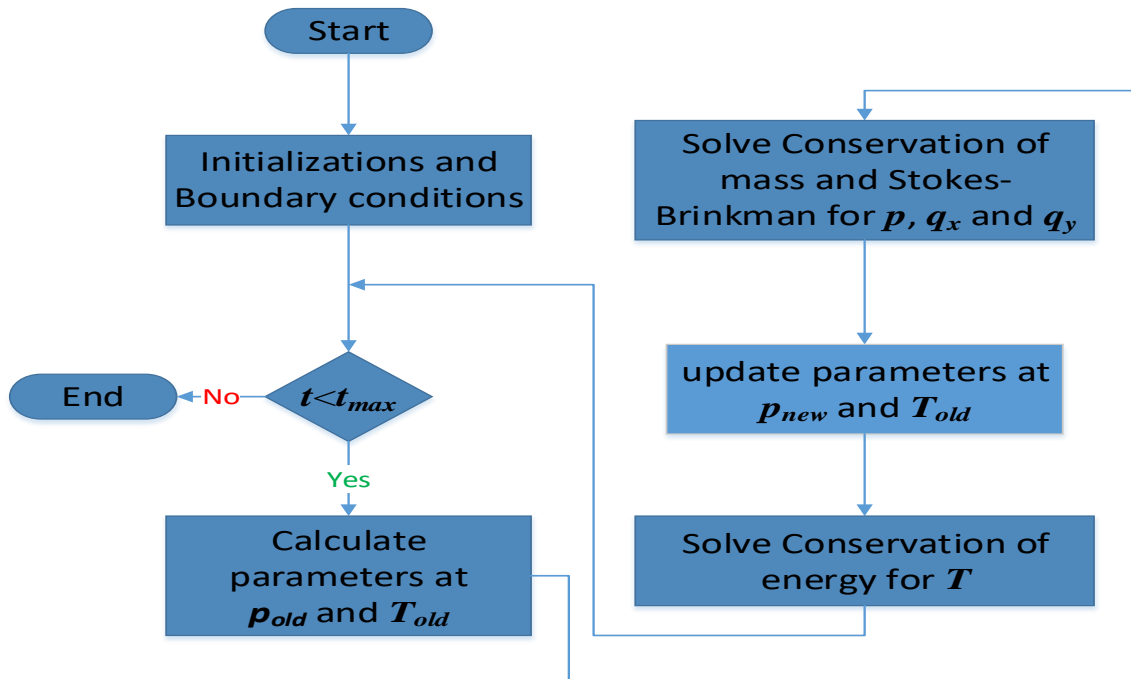


Figure 3 Flow chart of solution steps

3.3.Darcy Model with Estimated Permeability Distribution (DMEPD)

We introduce an alternative approach to model fluid flow in karst reservoirs. This approach, named Darcy Model with Estimated Permeability Distribution (DMEPD), is

simple and computationally less expensive than the Stokes-Brinkman model. The approach does not use the interface conditions that are implemented in Darcy-Stokes approach. Rather, the approach involves pre-calculating the apparent permeability values in the free-flow region and in the surrounding porous media (where the boundary layer is effective) from the analytical solution of Stokes-Brinkman's equation. Then, using Darcy's law to simulate fluid flow in karst reservoirs.

The first step in the DMEPD approach is to calculate the apparent permeability of the free-flow region grids and the surrounding porous media. Then, the permeability is distributed in the free-flow region and in the porous media around it. Using this technique, karst reservoirs and aquifers are simulated using Darcy's law instead of previous approaches.

3.3.1. Analytical solution

The analytical solution of Equation (2.7) was first introduced by Neale and Nader [15]. Their solution was only introduced for a channel that has a no-slip boundary condition on one side and a porous media on the other side. This solution was extended to account for periodic porous media with the same properties surrounding the free-flow region [19]. The previous two approaches considered the continuity of the velocity at the interface between the free-flow region and the porous media, however, both considered the apparent velocity as the actual velocity in the porous media. The approach presented in this research follow the same procedure, except that it assumes different properties of each porous media around the free-flow region as shown in Figure 4. Also, it is considered the continuity of the actual velocity (which it is different from apparent velocity) by implementing a jump between v_x (velocity along interface in free flow region) and u_x (superficial velocity along

interface in porous media). The domain is composed of a free-flow region with width W and surrounded by porous media on both sides. The porous media on each side has its own properties (k, ϕ, μ^*) different from those on the other side of the channel. The analytical solution is given by: -

$$\begin{cases} u_{x_1} = c_3 e^{-\lambda_1 y} - \frac{k_1}{\mu} \frac{\partial p}{\partial x}, & y > w \\ v_x = \frac{1}{\mu} \left(\frac{\partial p}{\partial x} 0.5 y^2 + c_1 y + c_2 \right), & 0 < y < w, \\ u_{x_2} = c_4 e^{\lambda_2 y} - \frac{k_2}{\mu} \frac{\partial p}{\partial x}, & y < 0 \end{cases} \quad (3.9)$$

where C_1, C_2, C_3 and C_4 are coefficients to the solution of the Stokes-Brinkman's differential equations. Note that the free-flow region extends from $y > 0$ to $y < w$, the upper porous media (Porous Media 1) extends from $y > w$ towards $+\infty$, and the lower porous media (Porous Media 2) extends from $y < 0$ towards $-\infty$. The interfaces between the cave and the two-porous media are at $y = 0$ and $y = w$. The details of this solution (Equation (3.9)) is presented in Appendix. Equation (3.9) shows that the boundary shear layer deteriorates exponentially as we move deeper into the porous media. It is also clear that the location of the maximum velocity is not necessarily located at the center of the channel, but shifted towards the porous media with a higher value of $\mu^* k$ (see Appendix for more details).

The velocity in Equation (3.9) can be used to calculate the equivalent permeability of any grid in the flow direction (x -direction in this case). The equivalent permeability of any grid cell that extends in the y -direction between any two points y_j and y_{j+1} is given by: -

$$k_{y_j \rightarrow y_{j+1}} = \frac{-\mu \int_{y_j}^{y_{j+1}} u_x dy}{(\partial p / \partial x) \int_{y_j}^{y_{j+1}} dy}. \quad (3.10)$$

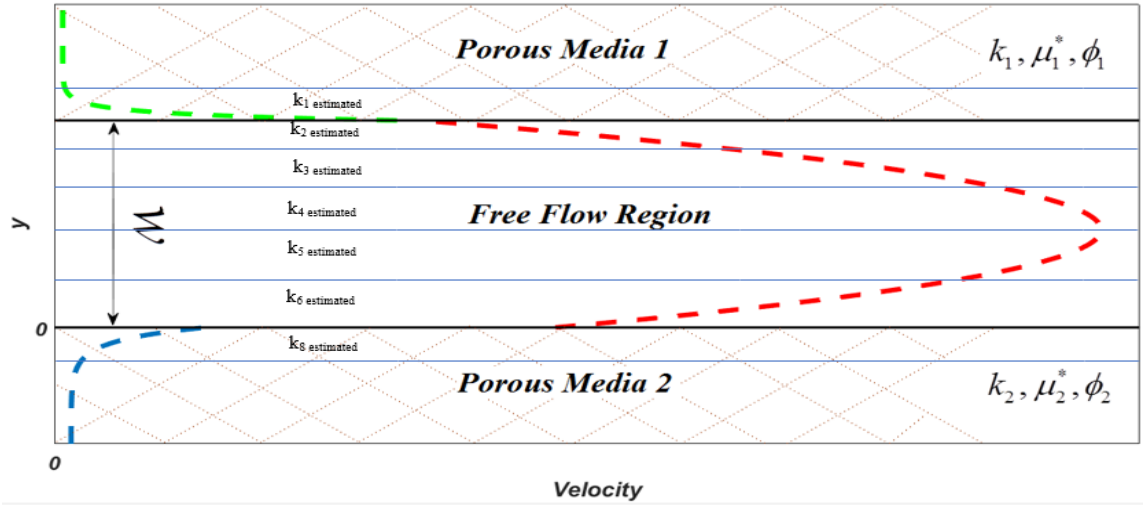


Figure 4 Apparent velocity distribution for a channel surrounded by porous media on each side.

In Equation (3.10), $k_{y_j \rightarrow y_{j+1}}$ is a volume-averaged permeability (in x -direction) obtained by averaging apparent velocity over the volume of a grid cell. In arriving at Equation (3.9), we have assumed that $\partial p / \partial x$ is constant throughout the system and that the cross-sectional area of free flow region does not vary. The Equation is applicable to both the free-flow region and the porous media. For any grid inside the free-flow region ($0 < y < w$), the equivalent permeability is calculated by substituting the appropriate expression for v_x from Equation (3.9) into Equation (3.10) to obtain: -

$$k_{y_j \rightarrow y_{j+1}} = \frac{-(y_j^2 + y_{j+1}^2 + y_j y_{j+1})}{6} - \frac{c_1 (y_j + y_{j+1})}{2 \partial p / \partial x} - \frac{c_2}{\partial p / \partial x}, \quad (3.11)$$

If we assume that $\mu_1^* = \mu_2^* = \mu$ and $k_1 = k_2 = k_{pm}$, the effect of the slip velocity on the channel permeability becomes crucial only when $k_{pm}/k_{pois} \geq 10^{-4}$, where $k_{pois} = w^2/12$ is the channel average permeability calculated from Poiseuille's equation with no-slip boundaries. This is evident in Figure 5 where k_{app}/k_{pois} is plotted against k_{pm}/k_{pois} (where k_{app} is the apparent permeability of the free-flow region). In the figure, we observe that when k_{pm}/k_{pois} is less than 10^{-4} , the plot is almost flat indicating that below this value, k_{app}/k_{pois} exhibits no noticeable change with k_{pm}/k_{pois} . Thus, in this range, the Poiseuille's equation can be used in place of the Stokes-Brinkman's equation. This result indicates that, it is only practical to use Stokes-Brinkman in the calculation of the apparent permeability of the free-flow region when the previous condition is satisfied and apart from that it is more practical to use Poiseuille's equation instead. Also, this result is in strong agreement with the results that generated by using numerical simulation by Krotkiewski [22].

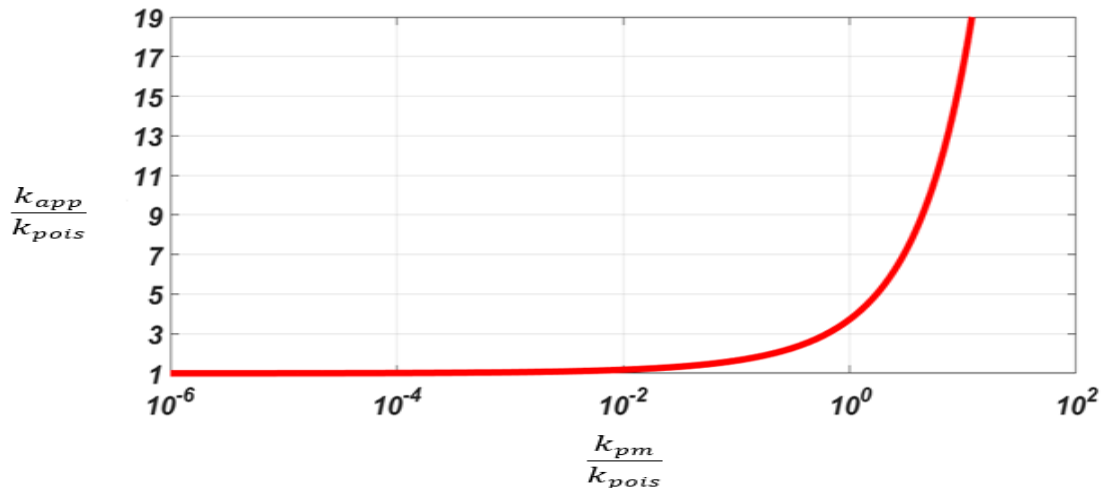


Figure 5 Variation of apparent channel permeability with respect to Darcy permeability at different ratios of porous media permeability with respect to channel Darcy permeability.

Figure 6 shows the effect of $\xi = \mu/\mu^*$. When ξ decreases, the apparent permeability increases due to the increase of the actual velocity inside porous media.

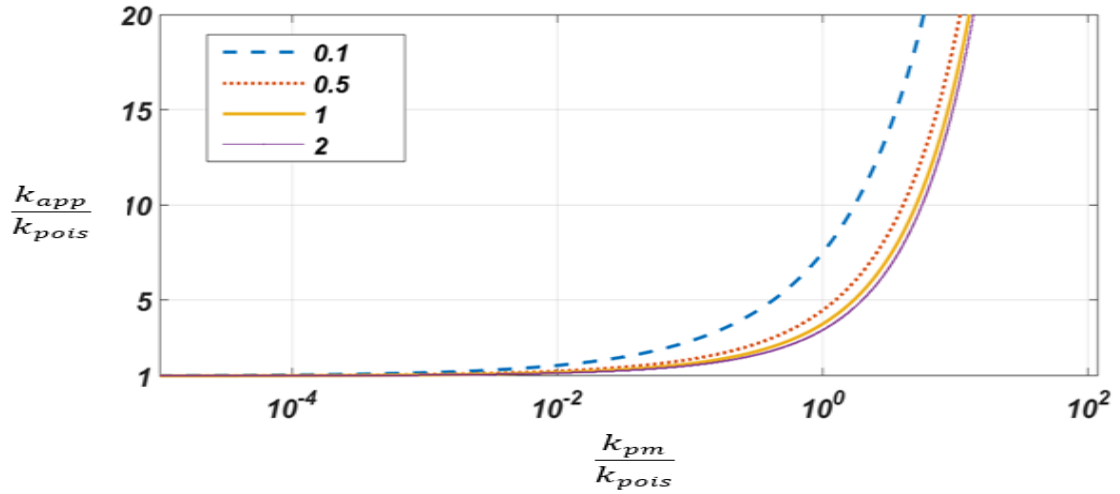


Figure 6 Effect of $\frac{\mu}{\mu^*}$ on the calculated apparent permeability.

One problem with the DMEPD method is that in the case of free-flow regions with large widths ($k_{pm} \square 10^{-4} k_{pois}$), the estimated permeability inside free-flow region is very high.

In this case, the very large contrast between the permeability in the free-flow region and that in the porous region causes the coefficient matrix of the resulting linear system to be ill-conditioned. To reduce this effect, a weighted version of DMEPD known as Darcy's model with weighted estimated permeability distribution (DMWEPD) is proposed. In DMWEPD, a suitable weighting factor (between zero and one) is multiplied by the estimated free-flow region permeability during the pressure calculation step. Then, after calculating the pressure, the rate is calculated using original permeability computed from the analytical solution. This technique reduces the ratio between maximum eigenvalue and

minimum eigenvalue in transmissibility matrix and thus stabilizes the linear system. The flow charts of DMEPD and DMWEPD are shown in Figure 7 and Figure 8.

3.3.2. Flow in Caves Not Aligned with the Principal Direction of Flow

The analytical solution presented in Subsection 3.3.1. gives the apparent permeability in the direction of the free-flow region. However, in reality, the flow direction in the caves do not necessarily align with the proposed system direction of flow in the reservoir. For such cases that contains free-flow region not aligned with principle direction, there are two approaches. The first approach is considering unstructured gridding where the grids inside the free-flow region are aligned with the direction of the cave. The second approach is to use the full tensor permeability.

This work considers that all the grids are aligned with the principal directions of permeability in the porous media. Therefore, the full permeability tensor is used to handle the non-alignment of the free-flow region with the system directions. Many methods are found in the literature that deal with simulation using full tensor permeability using multipoint flux approximation (see [52-55]). Majority of these methods suffer from non-monotonicity problem [56,57] which is not suitable in our case due to the high contrast between permeabilities of the principle directions in the free-flow region (one direction is aligned with the free-flow region and the other is perpendicular to it). A recent method known as globally-coupled pressure method (GCP) does not face this issue in the case of no-flow external boundaries. However, the method also suffers from the non-monotonicity problem when constant-pressure boundaries are imposed. Nonetheless, the globally-coupled pressure method was shown to be the more efficient than the other multipoint flux approximation methods and we adopt this method in this work.

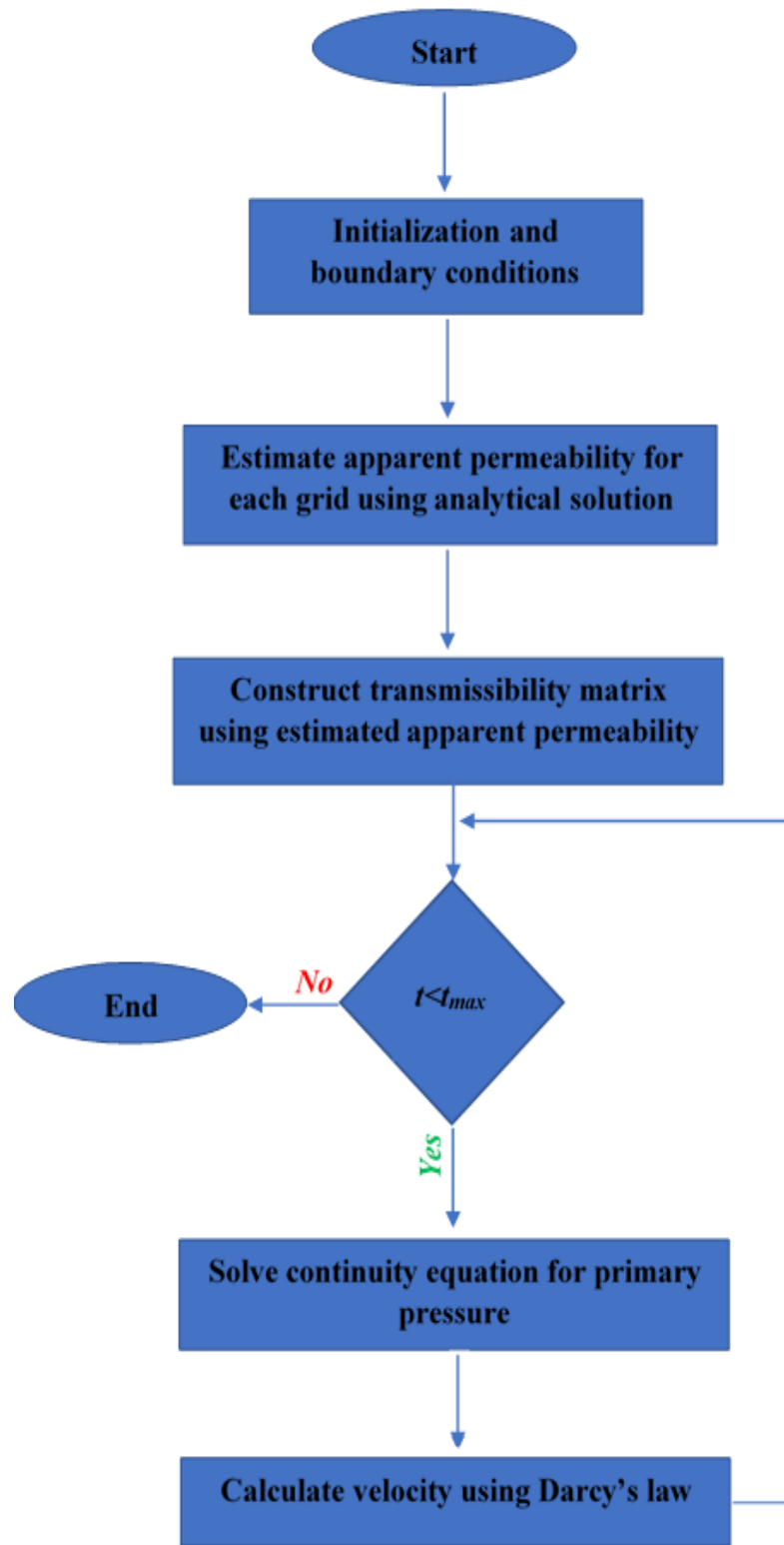


Figure 7 Flow chart of DMEPD

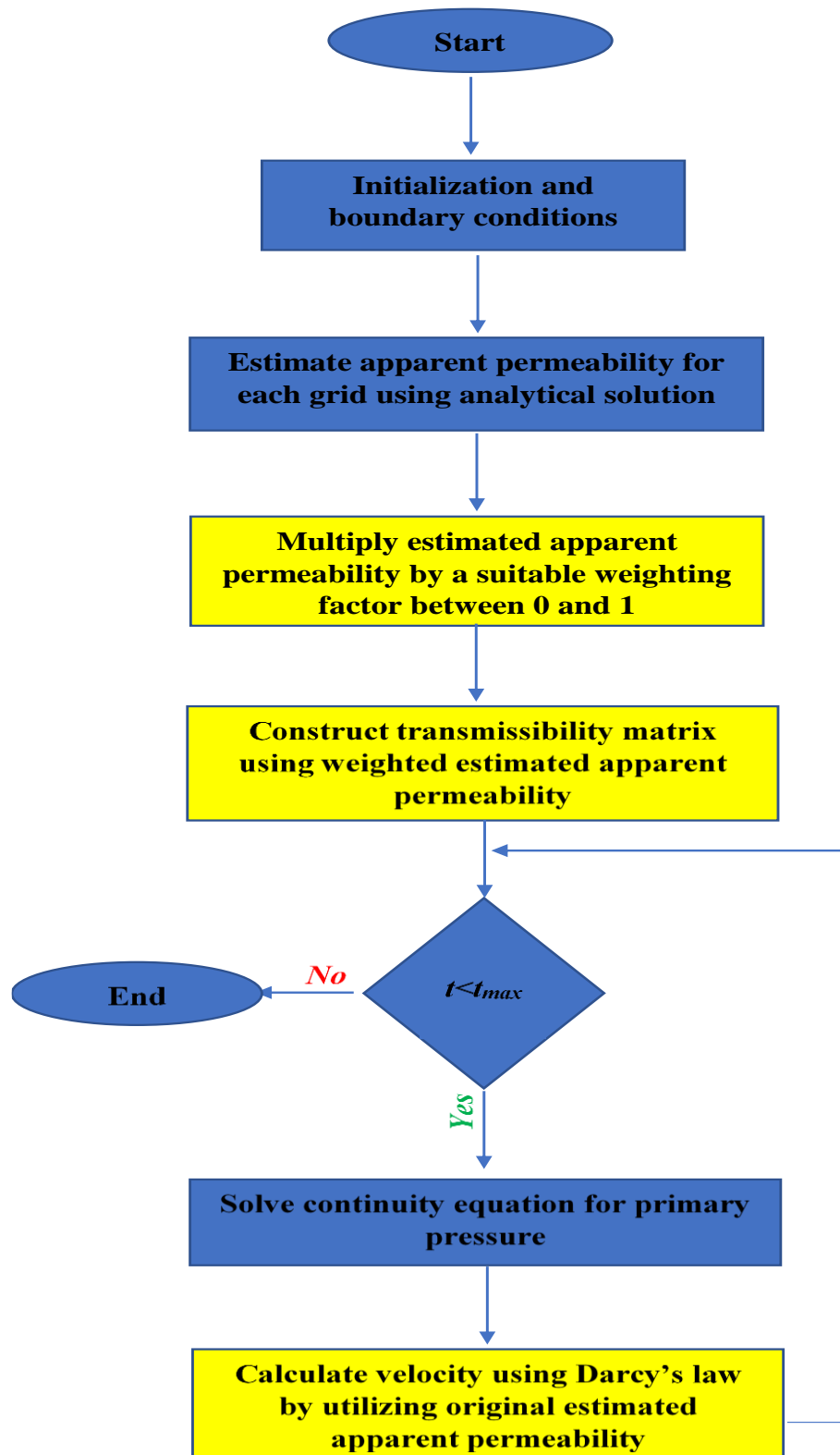


Figure 8 Flow chart of DMWEPD

The globally-coupled pressure method relies on introducing auxiliary pressure unknowns at the centroid of the interface between grids, and then imposing flux continuity across the interfaces between grids as shown in Figure 9 which considers two adjacent grids labelled 1 and 2. The flux from Grid-1 toward Grid-2 can be calculated as the component of the velocity in the x -direction as: -

$$f_{x_1} = (\mathbf{u}_1 \cdot \mathbf{i}) A_x, \quad (3.12)$$

where the velocity is calculated from Darcy's law as: -

$$\mathbf{u}_1 = -\frac{1}{\mu_1} \overline{k}_1 \cdot \nabla p_1, \quad (3.13)$$

where $\nabla p_1 = \left(\frac{p_x - p_1}{\Delta x_1 / 2} \quad \frac{p_{y_1} - p_1}{\Delta y_1 / 2} \right)$. The flux from Grid-2 toward Grid-1 is computed in similar manner and then, from the flux continuity across interface between two grids we have: -

$$f_{x_1} + f_{x_2} = 0. \quad (3.14)$$

The linear system of equations between the primary pressures at the center of the grid blocks and the auxiliary pressures at the interfaces can be stated as: -

$$S \overline{\mathbf{p}} = W \mathbf{p}, \quad (3.15)$$

where $\overline{\mathbf{p}}$ is the vector of auxiliary pressure unknowns (e.g. p_x and p_{y_1}), S is an $N_f \times N_f$ matrix composed of the coefficients of the auxiliary pressures, and W is an $N_f \times N_c$ matrix

that contains the coefficients of the primary pressures. Then, the fluxes through the interfaces can be written as: -

$$\mathbf{f} = R\bar{\mathbf{p}} + E\mathbf{p} = R(S^{-1}L\mathbf{p}) + E\mathbf{p} = T\mathbf{p}, \quad (3.16)$$

where T is the transmissibility matrix. Equation (3.16) can be used to replace the flux by primary pressure in the conservation of mass equation. Further information can be obtained from [58]. The GCP method used in this work models flow in the caves with a reasonable degree of accuracy. However, the main disadvantage of this approach is that the transmissibility matrix contains many non-zero entries due to the large flux stencil, thus increasing the computational complexity of the model.

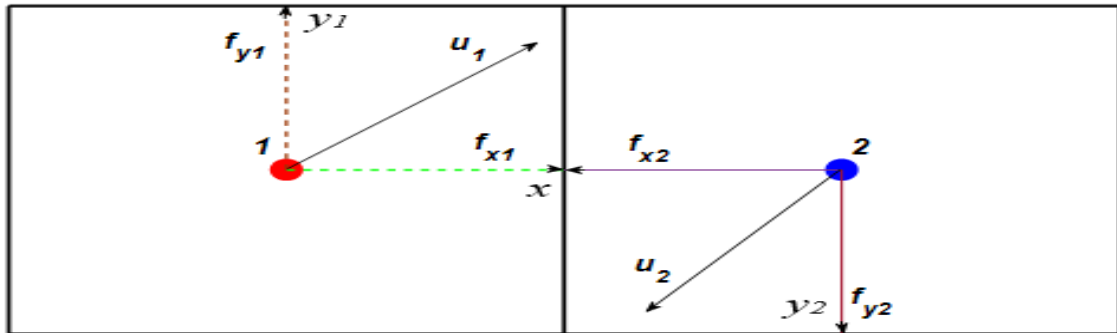


Figure 9 Flux continuity across interface between two grid blocks.

CHAPTER 4

Results, Discussion and Conclusion

The cases that are related to thermal simulation using Stokes-Brinkman's equation is presented first followed by the cases related to DMEPD. The numerical simulation is performed using mldivide operator $\mathbf{s} = \mathbf{A} \backslash \mathbf{b}$ in MATLAB (MATLAB and Statistics Toolbox Release 2015b, The MathWorks, Inc., Natick, Massachusetts, United States) on personal computer with a 2-core processor of Intel CoreTMi5-2450M CPU @ 2.5 GHz.

4.1. Application Examples of Thermal Flow Simulation in Karstic Media

Two examples are investigated and the results from both Stokes-Brinkman and Darcy models are compared.

4.1.1. Example 1 (Simple Model)

The aquifer parameters used in this example are presented on Table 2. Rectilinear gridding is used in y -direction to capture flow behavior inside and around the cave. In the y -direction, there are 6 divisions, each of $4ft$ inside the cave (Figure 10). The water viscosity and formation volume factor are slightly variable functions of pressure and temperature. There are two wells (one injector and a producer) located in the neighborhood of the cave. The injector injects relatively cold water while the producer produces hot water at a relatively high temperature. Water contains a small amount of dissolved gas about $30scf/stb$. Therefore, this little amount of dissolved gas has a negligible effect and hence it is assumed that $c_{p_f} = c_{v_f}$. The equivalent constant permeability of the grids inside the free-flow region in the second case is calculated from Poiseuille's equation to be

$4.5 \times 10^{15} \text{ md}$ for each of the grids. The outer boundaries of the aquifer are assumed to be sealed.

Table 2 Simple model parameters

Length (<i>ft.</i>)	4500	No. of grids in <i>x</i> direction	150
Width (<i>ft.</i>)	1728	Grid size in <i>x</i> direction (<i>ft.</i>)	30
Thickness (<i>ft.</i>)	15	No. of grids in <i>y</i> direction	18
Cave aperture (<i>ft.</i>)	24	Porous media porosity at standard conditions	0.18
Initial pressure (<i>psig</i>)	6000	Formation compressibility (psi^{-1})	10^{-6}
Initial temperature ($^{\circ}R$)	670	Porous media permeability (<i>mD</i>)	333
Producer grid index	(2,6)	Fluid density at standard conditions (lb / ft^3)	62.4
Injector grid index	(149,13)	Fluid thermal conductivity ($\text{BTU} / \text{d.ft.}^{\circ}R$)	8.016
Production rate	700 <i>STB</i> / <i>d</i>	Rock thermal conductivity ($\text{BTU} / \text{d.ft.}^{\circ}R$)	61.537

Injection rate	700 STB/d	Injected fluid temperature ($^{\circ}R$)	550
----------------	-----------	--	-----

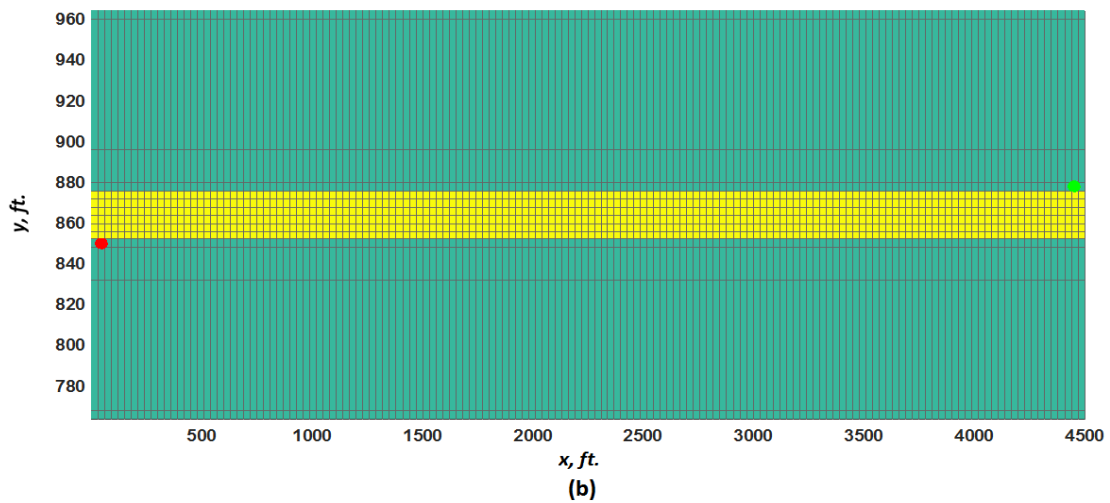
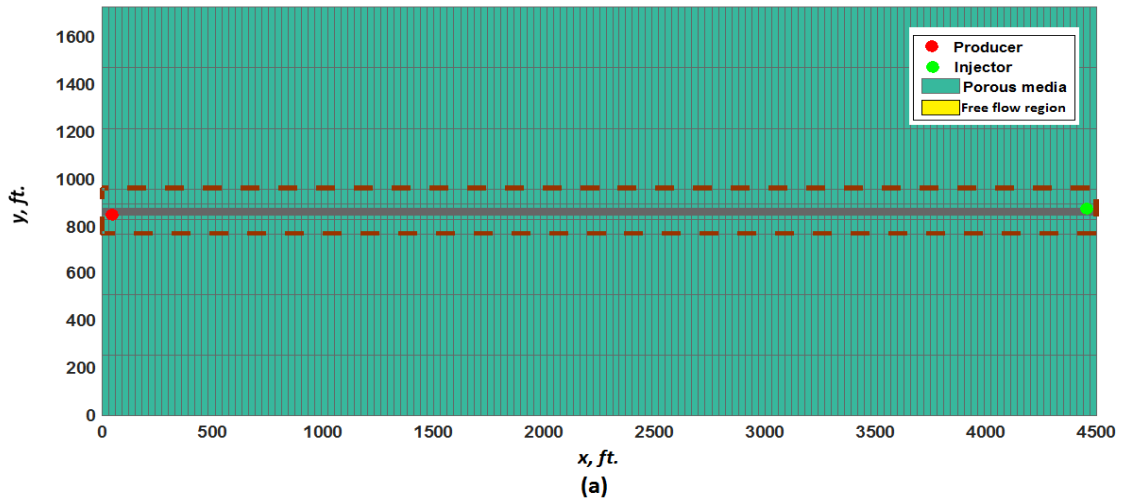


Figure 10 (a) Simple caved aquifer model (b) Magnification of the region surrounded by brown box

The Stokes-Brinkman model and the Darcy model separately were used to model the fluid flow in the aquifer and the results from these two models were compared. Figure 11 and Figure 12 show the aquifer temperature distribution after 100 days obtained from the Stokes-Brinkman model and Darcy model, respectively. It is evident from the two figures

that the heat front moves faster in Stokes-Brinkman model than in the Darcy model. Due to fast movement of the heat front in the Stokes-Brinkman model, the fluid temperature observed at the production well starts to decrease early in the Stokes-Brinkman model than in the Darcy model. Figure 13 shows that the temperature of the produced fluid from producer drops earlier in the Stokes-Brinkman model than in Darcy model.

Figure 14 indicates that decreasing grid cell size around the interface between porous media and free-flow region from 4 *ft.* to 0.5 *ft.* makes the model more accurate by increasing the velocity of the tip of the heat front compared with Figure 5. Also, small grid cells reduce effect of numerical dispersion. However, the increase in the accuracy with decreasing grid cells size around interface is not significant after certain limit beside increasing the computational cost dramatically. More clarification related to the effect of the gridding on Stokes-Brinkman's equation is mentioned later.

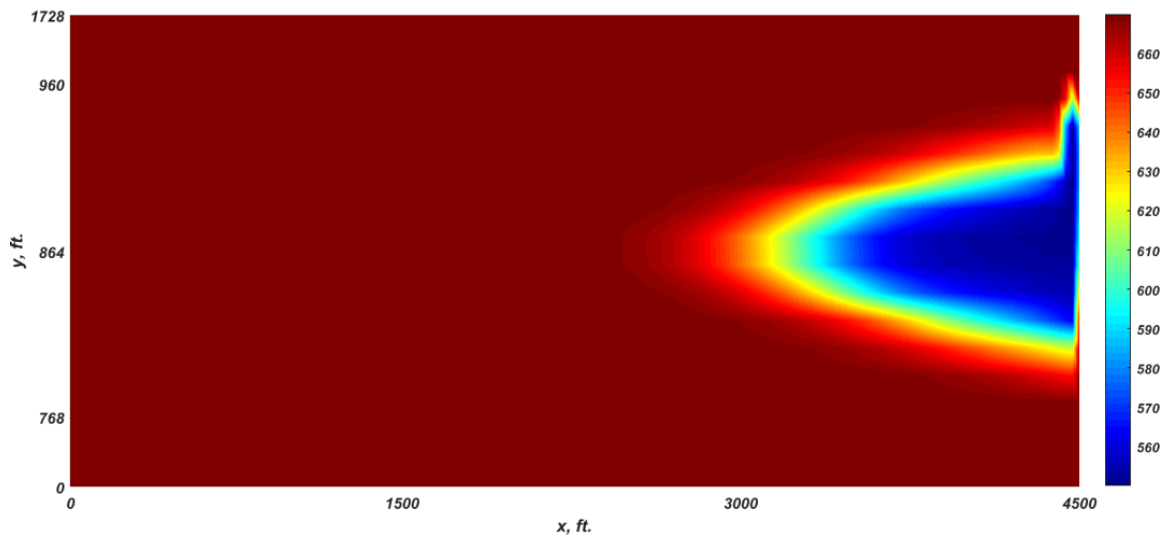


Figure 11 Temperature distribution in $^{\circ}R$ at 100 days using Stokes-Brinkman's model (Hint: - the sizes of all the grid blocks are equal for the sake of visualization)

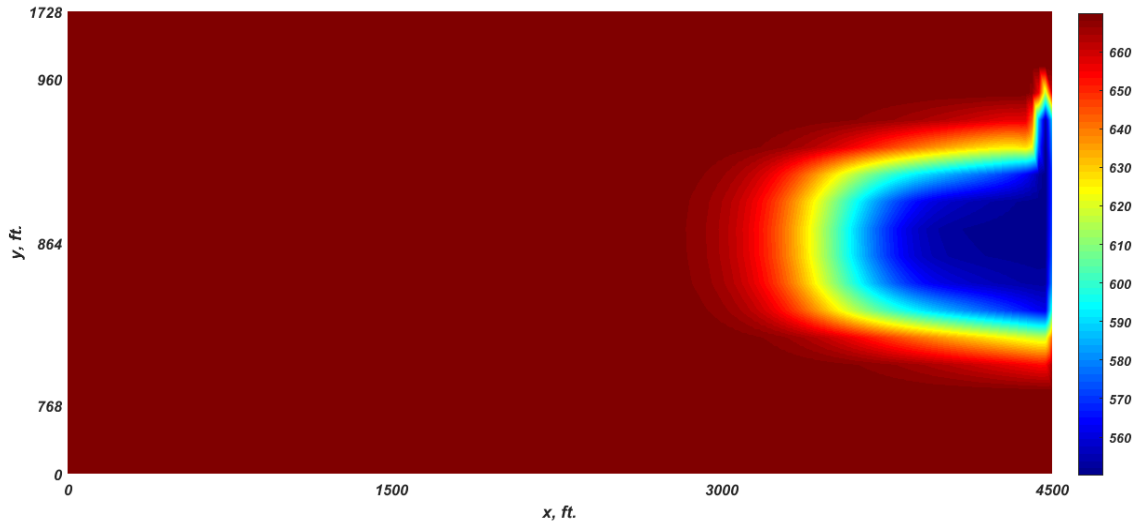


Figure 12 Temperature distribution in $^{\circ}R$ at 100 days using Darcy model (Hint: - the sizes of all the grid blocks are equal for the sake of visualization)

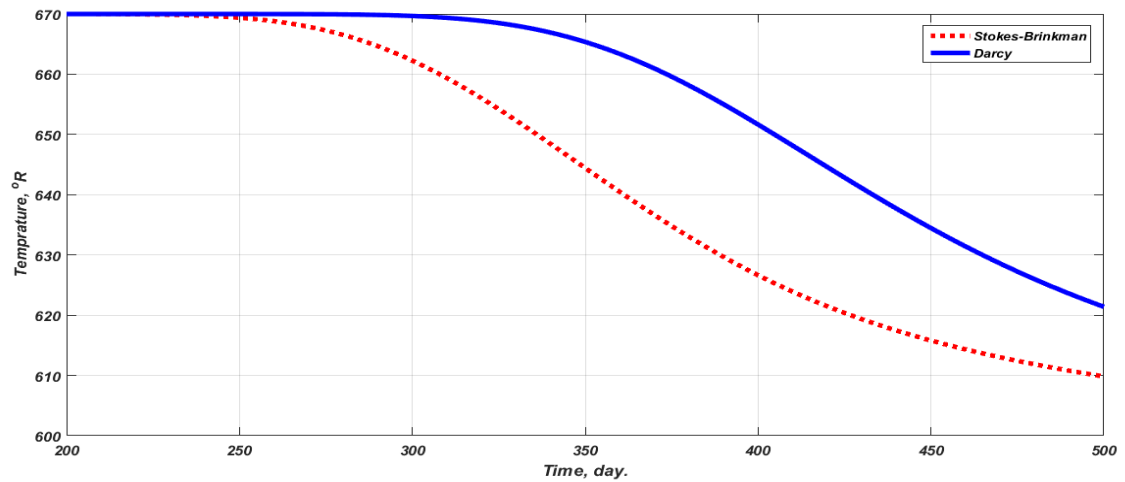


Figure 13 Temperature of the fluid produced from production well

4.1.2. Example 2

The second example involves a more complex aquifer model containing a cave ($12ft \times 10ft$) with two branches, and a heterogeneous permeability distribution within the porous media as shown in Figure 16. To properly observe the movement of the heat front,

a very fine gridding is used in and around the free-flow region. The fluid and rock properties are the same as used in Example 1 (Table 1).

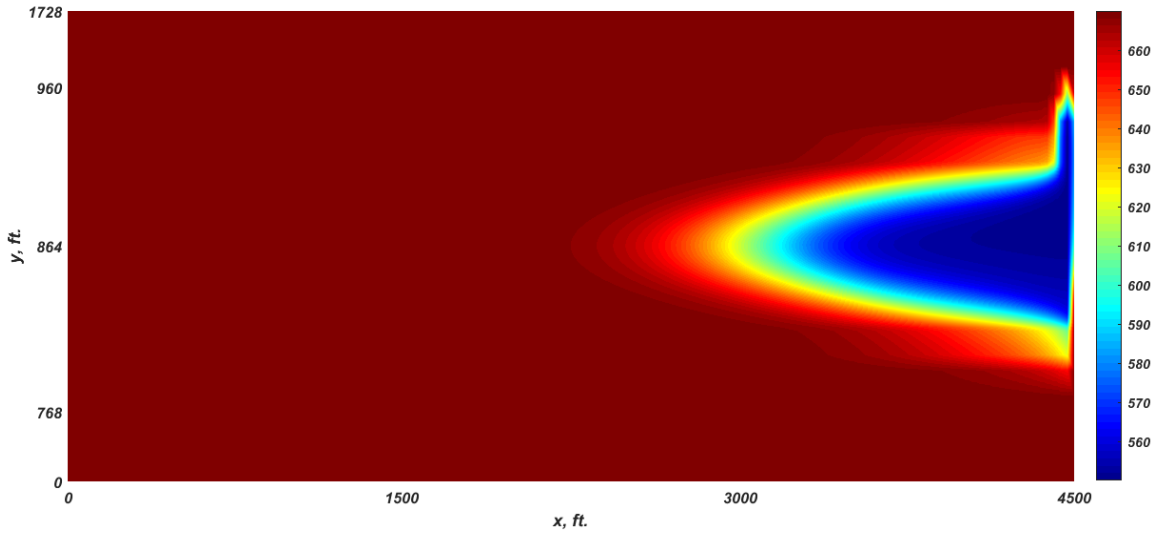


Figure 14 Temperature distribution in $^{\circ}R$ at 100 days using Brinkman's equation and grid width 0.5 ft. in y-direction around interface between porous media and free-flow region (Hint: - the sizes of all the grid blocks are equal for the sake of visualization)

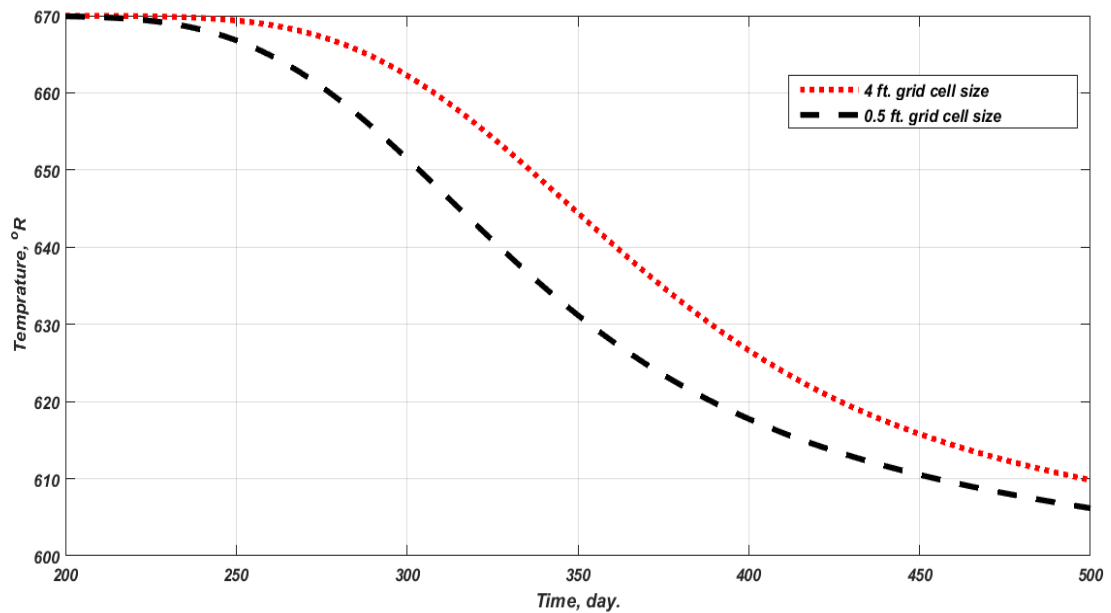


Figure 15 Effect of grid cells size around interface between porous media and free-flow region on the produced fluid temperature

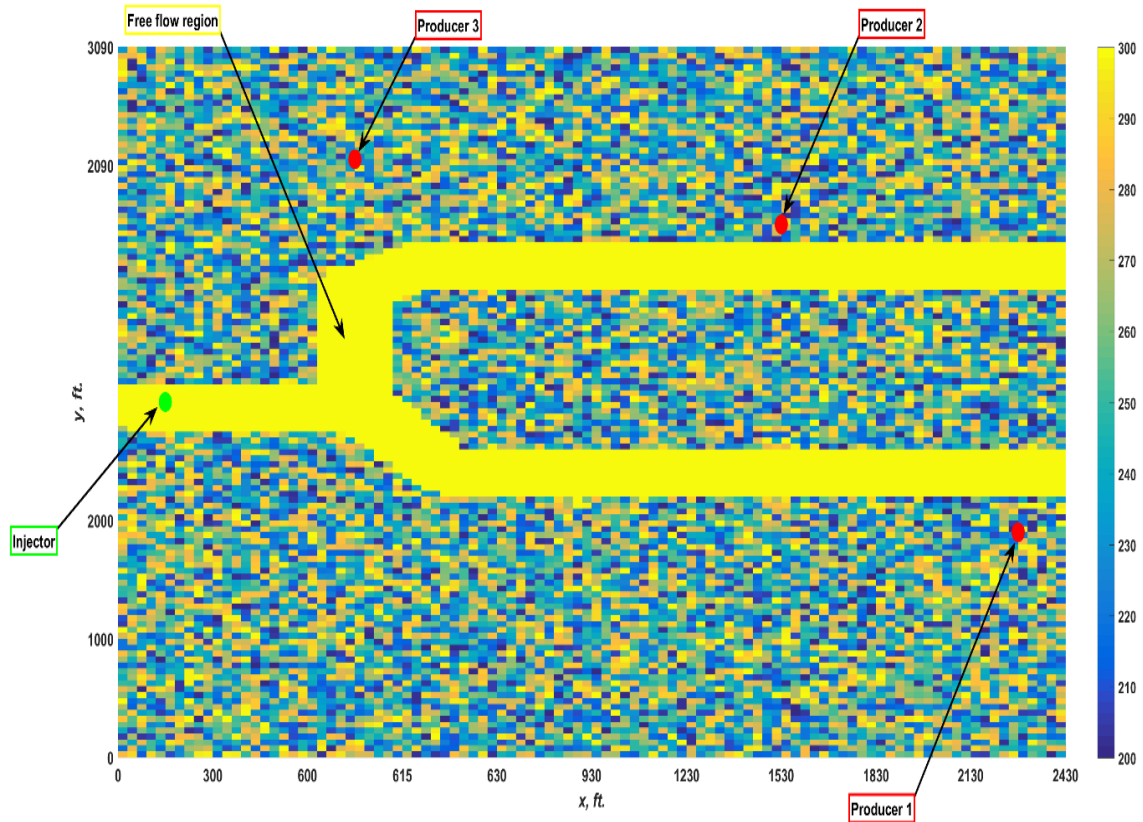


Figure 16 Permeability distribution in *md* of complicated caved aquifer model (Hint: - the cave is in yellow)

Figure 17 shows also that the temperature of the produced fluid from the producers decreases earlier in the Stokes-Brinkman model than in the Darcy model, except for the case of Producer 3, which is located inside the porous media far away from the free-flow region. Because the thermal conductivity of porous media is about 8 times larger than the fluid's thermal conductivity, thermal conduction will dissipate energy inside porous media. Also, the difference in temperature between the two models is insignificant in the case of Producer 1. Therefore, there is negligible difference in produced fluid temperature between Darcy and Stokes-Brinkman models for the wells that are located in the porous media and far from the cave, due to dispersion of the energy caused by diffusion.

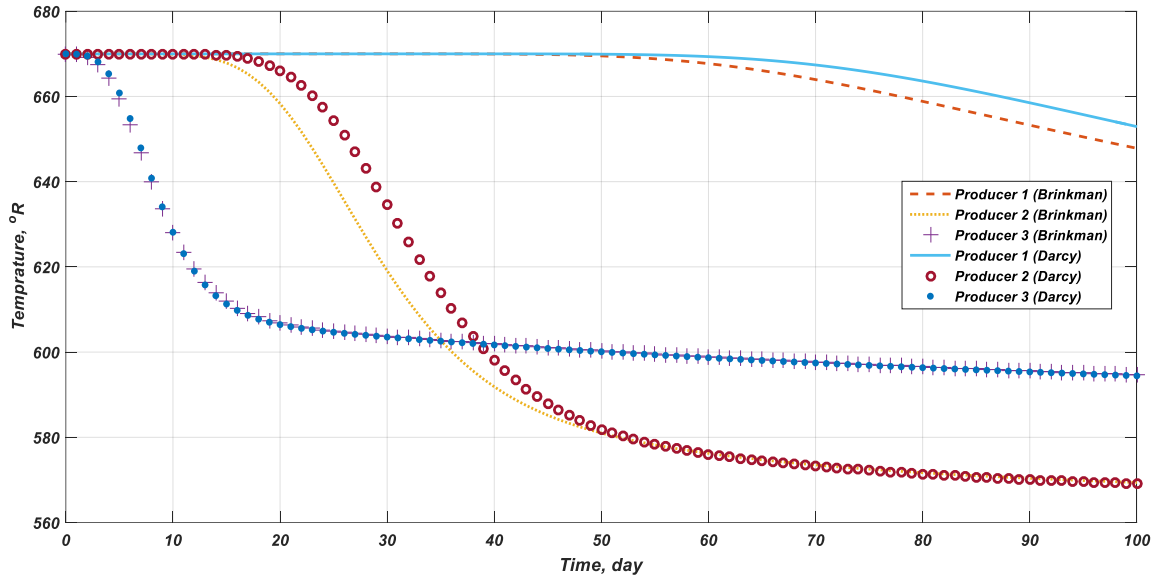


Figure 17 Produced fluid temperature from production wells (complicated model)

4.2. Sample Applications of DMEPD

Four cases are investigated and the numerical results using finite-volume discretization from both the DMEPD and DMWEPD approaches are compared with Stokes-Brinkman and with analytical solution in the first two cases.

4.2.1. Example 1: Channel Flow

This example presents a simple straight channel with constant pressure boundaries in x -direction and no-flow boundaries in y -direction and the fluid is incompressible. This case is tackled as a matter of validation due to the existence of analytical solution. The estimated permeability distribution that is used for the DMEPD is shown in Figure 18. The results presented in Figure 19 show that the velocity profile obtained from numerical simulation using both of DMEPD is in a good agreement with both the simulation using Stokes-Brinkman and the analytical solution of Stokes-Brinkman's equation. 100 runs with different numbers of grids were performed to evaluate the performance of DMEPD and

Stokes-Brinkman. Due to the existence of fluxes at the boundaries of the grids as primary unknowns the size of the coefficient matrix in Stokes-Brinkman’s approach is larger than the one associated with DMEPD. The high-low-close diagram presented in Figure 20 reveals the significant reduction in time of simulation when DMEPD is used instead of Stokes-Brinkman. A larger reduction in time is observed as the number of grid blocks increases.

4.2.2. Example 2: Underground River

In Example 2, we consider flow of water in an underground river. The free-flow region is surrounded from two opposite banks by porous media. The permeability distribution in the DMEPD is shown in Figure 21. Figure 22 presents comparison between the apparent velocity profile generated by different methods. Again, the results show perfect match between analytical solution and both DMEPD and DMWEPD. The selected weighting factor is 10^{-6} which increases $\frac{|\lambda(T)|_{\min}}{|\lambda(T)|_{\max}}$ (where $\lambda(T)$ are the eigenvalues of transmissibility matrix) from 9.3×10^{-18} to 7.8×10^{-12} .

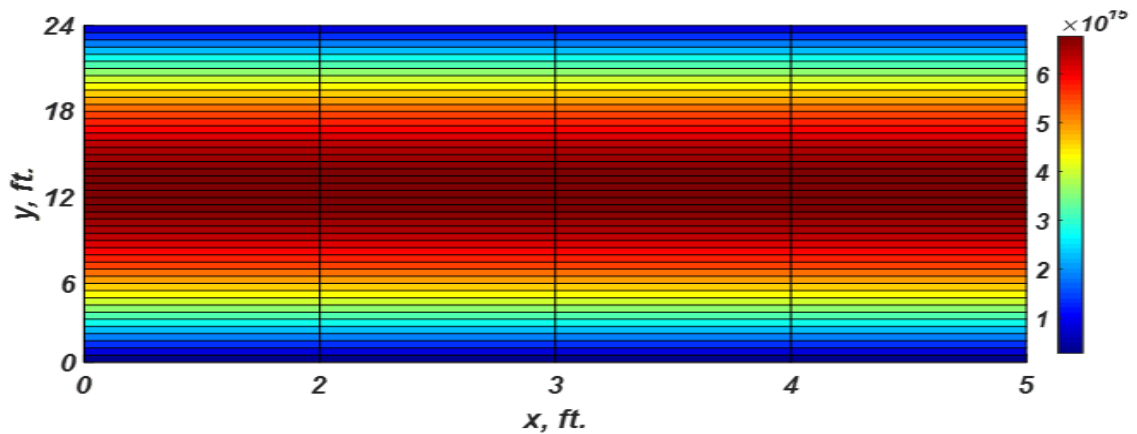


Figure 18 Estimated permeability (mD) distribution calculated from analytical solution for DMEPD of the channel flow case.

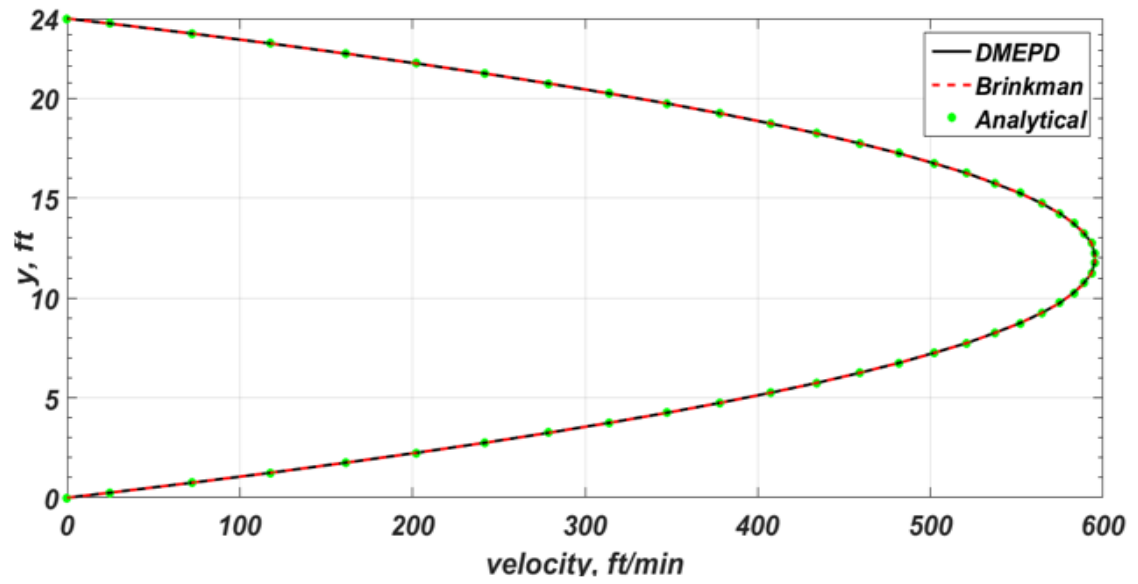


Figure 19 Velocity profile for channel case using different approaches.

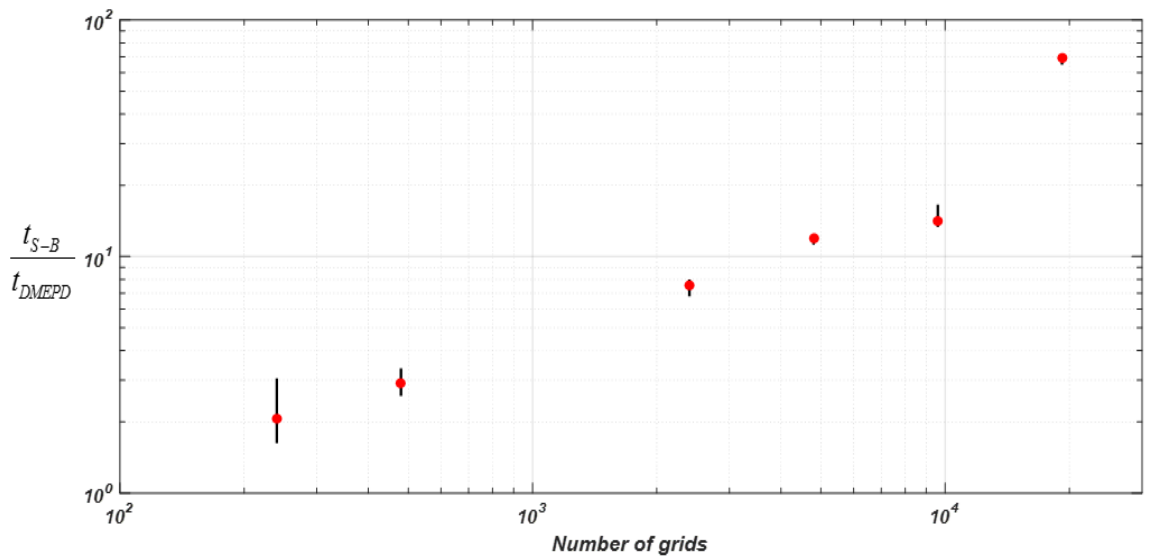


Figure 20 Variation of $\frac{t_{S-B}}{t_{DMEPD}}$ with model number of grids.

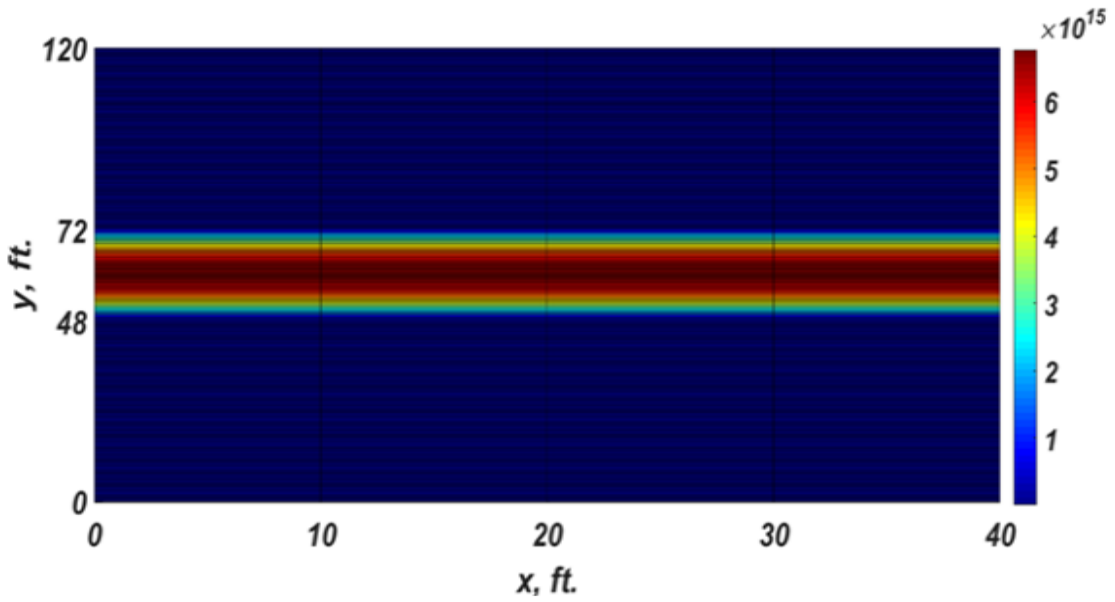


Figure 21 Estimated permeability distribution (md) of underground river case

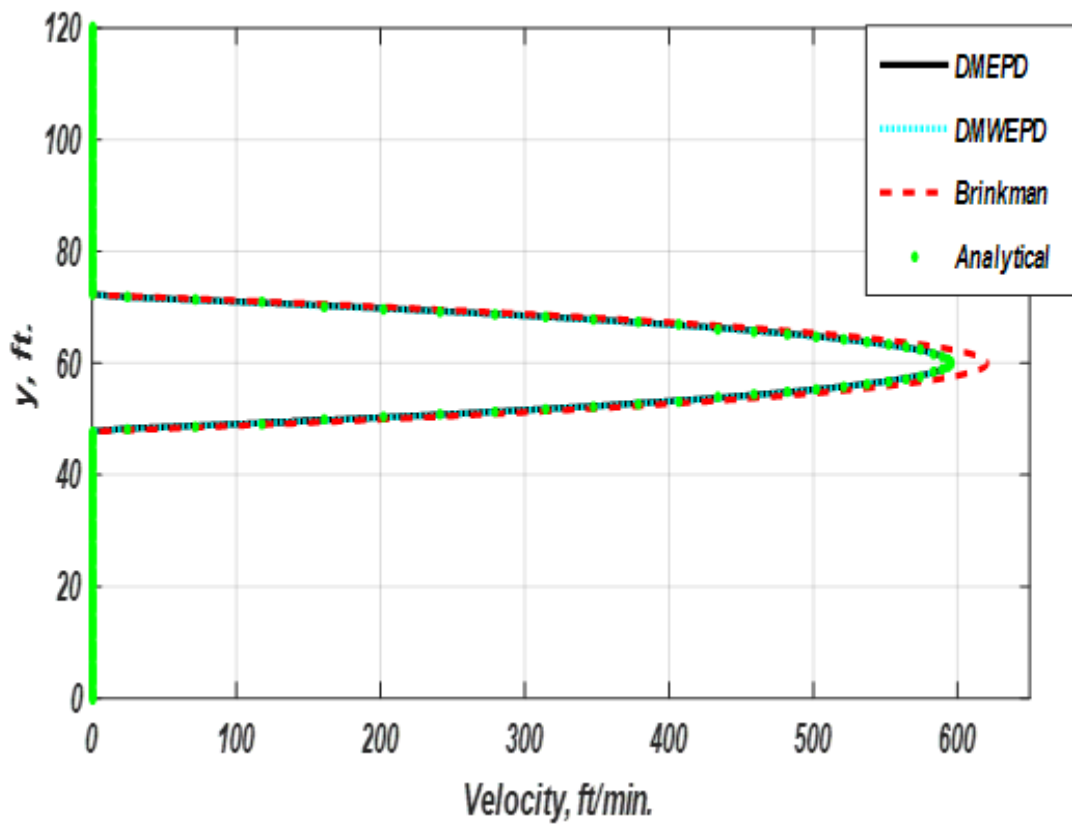


Figure 22 Velocity profile for underground river case using different approaches.

The velocity profile calculated from Stokes-Brinkman's exhibits a little deviation compared with analytical solution. Further runs are carried out with different grid widths in y-direction for the grids in the free flow region and for those in porous media close to interfaces. It is obvious from Figure 23 that Stokes-Brinkman model is highly affected by the grids dimensions. These differences are due to effect of the discretization of the second order Laplacian term around the interfaces between the porous media and the free flow region. Although it is well-known from the literature and from the analytical solution that the velocity deteriorates quickly (of order \sqrt{k} and exponential decay) inside the porous media, in the discretized domain the velocity feels the apparent interfaces at the center of the porous media grids neighbor to the free flow region not at the actual interfaces like if the size of the free flow region is extended. Hence, as Stokes-Brinkman contains a second order shear term which is discretized around interface, Stokes-Brinkman's models are greatly sensitive to width of grids around interface as shown in Figure 23. Figure 24 gives a closer look to the velocity distribution around the interfaces for different grid widths using Stokes-Brinkman. It is also predicted from Figure 24 that the no-slip boundary conditions force the velocity to be reduced to zero at the boundaries which is not consistent with Darcy's law and needs very fine gridding to reduce this effect. Figure 25 validates the hypothesis of the apparent increase in the area of the free flow-flow region when utilizing Stokes-Brinkman's equation for simulating large widths. It is clear from the diagram that anticipated max velocity using Stokes-Brinkman $(v_{S-B})_{\max}$ is higher than the expected velocity expected max velocity using Poiseuille's equation with actual free-flow region width which can be calculated from the following equation: -

$$u_{pois_{max}} = -\frac{w^2 \Delta p}{8\mu \Delta x}. \quad (4.1)$$

However, the max velocity using Stokes-Brinkman's equation is nearly the same as that expected from analytical solution with the width of the free flow region is apparently expanded to the center of the neighbor grids to the interface in the porous media. Then, the max apparent velocity can be calculated as following: -

$$u_{pois_{max}} = -\frac{(w + w_{grid})^2 \Delta p}{8\mu \Delta x}. \quad (4.2)$$

DMEPD has the advantage of not suffering from the effect gridding neither near the boundaries nor close to interfaces as it is shown in both Figure 26 and Figure 27 which indicates the unnecessary use of fine gridding with DMEPD.

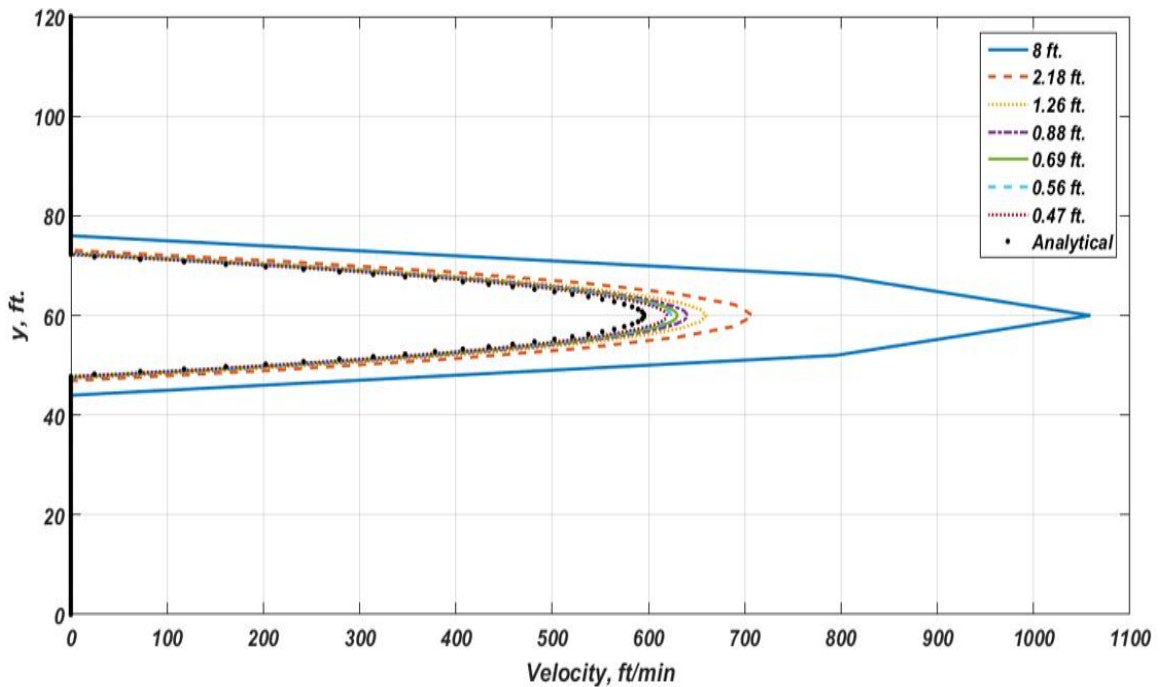


Figure 23 Velocity profile using Stokes-Brinkman at different grid width.

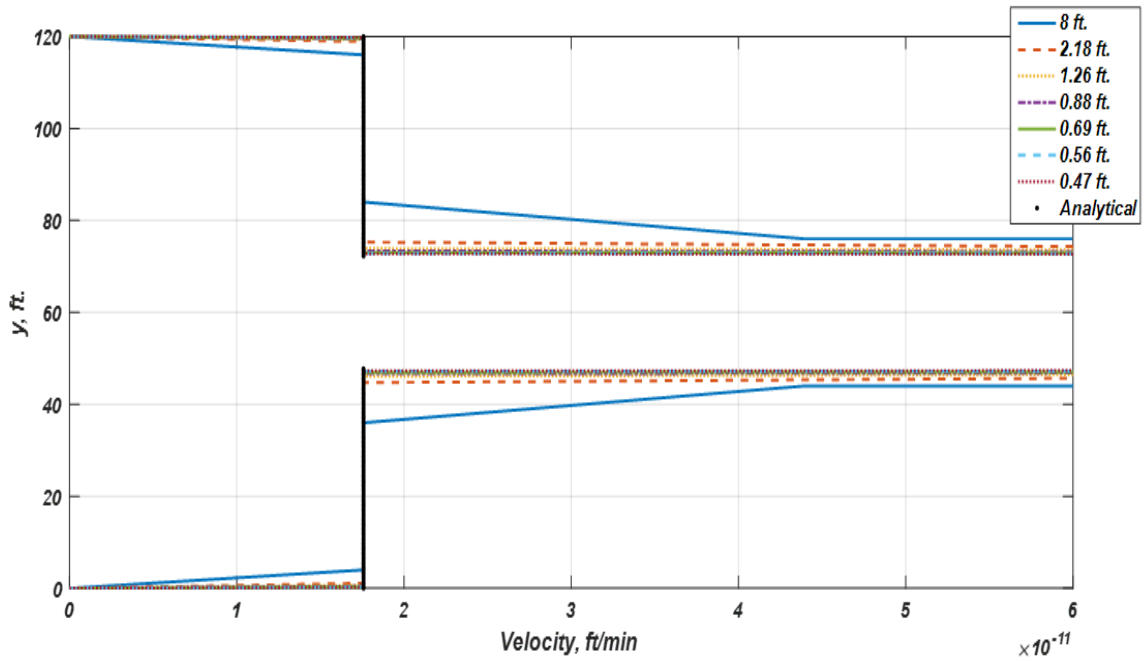


Figure 24 Velocity profile near the interfaces and boundaries using Stokes-Brinkman at different grid width.

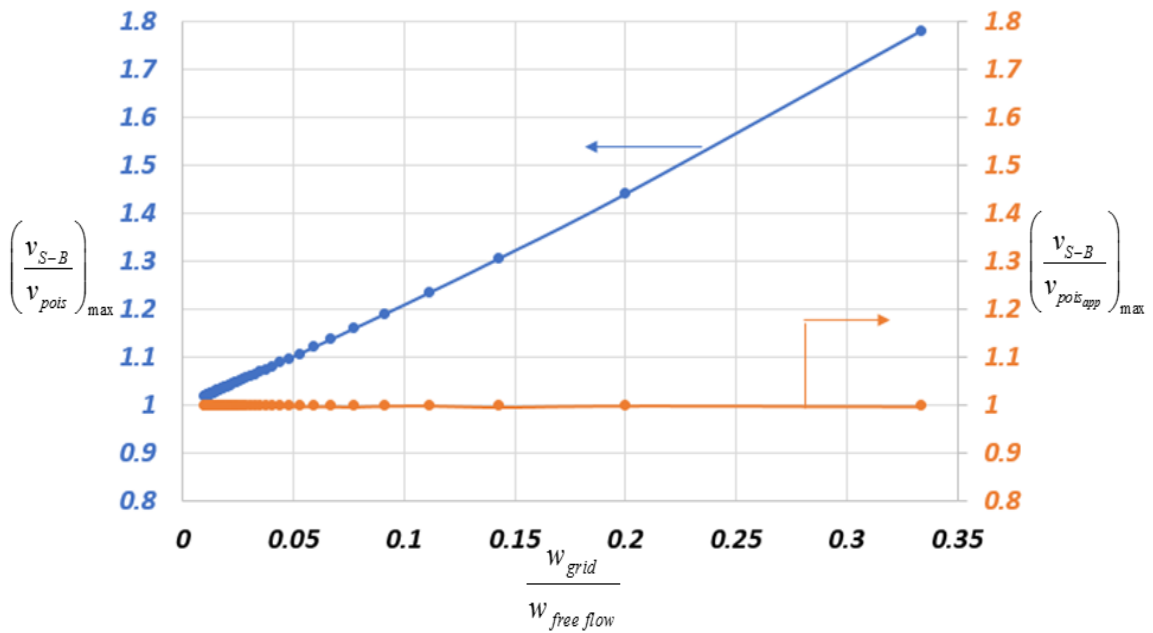


Figure 25 Ratio of max anticipated velocity using numerical Stokes-Brinkman to max Poiseuille's velocity using actual area of free flow region and apparent area (start from center of first grid inside porous media adjacent to interface) at various grid widths.

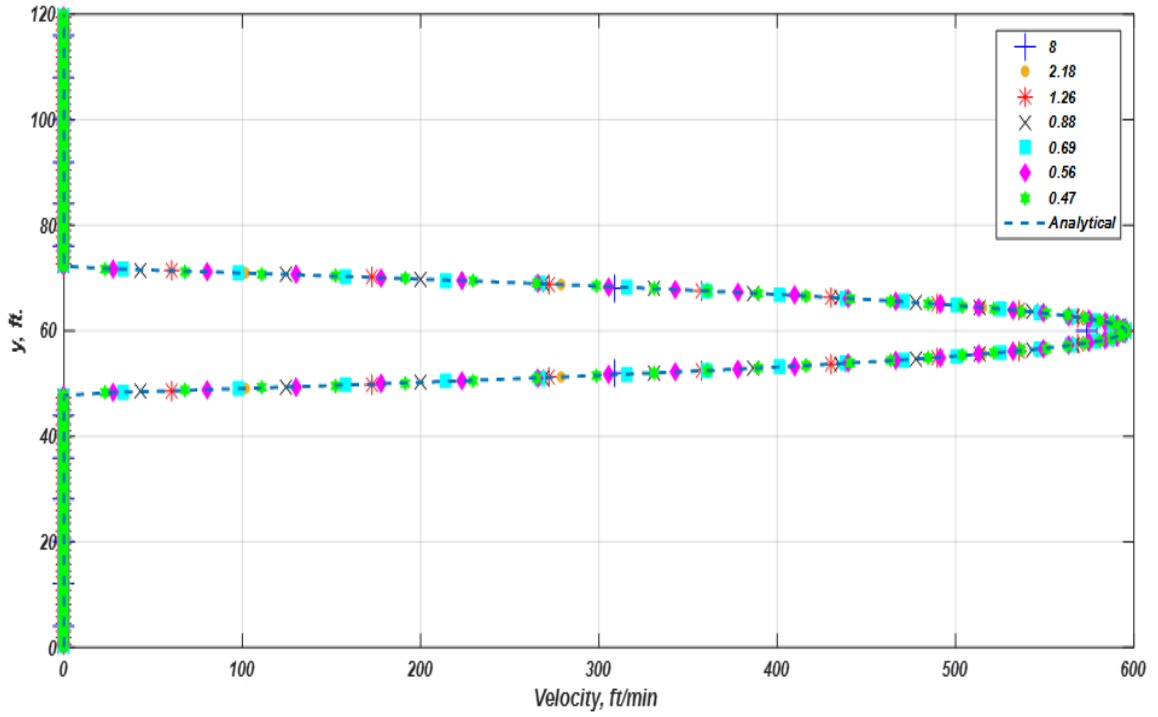


Figure 26 Velocity profile using DMEPD at different grid width.

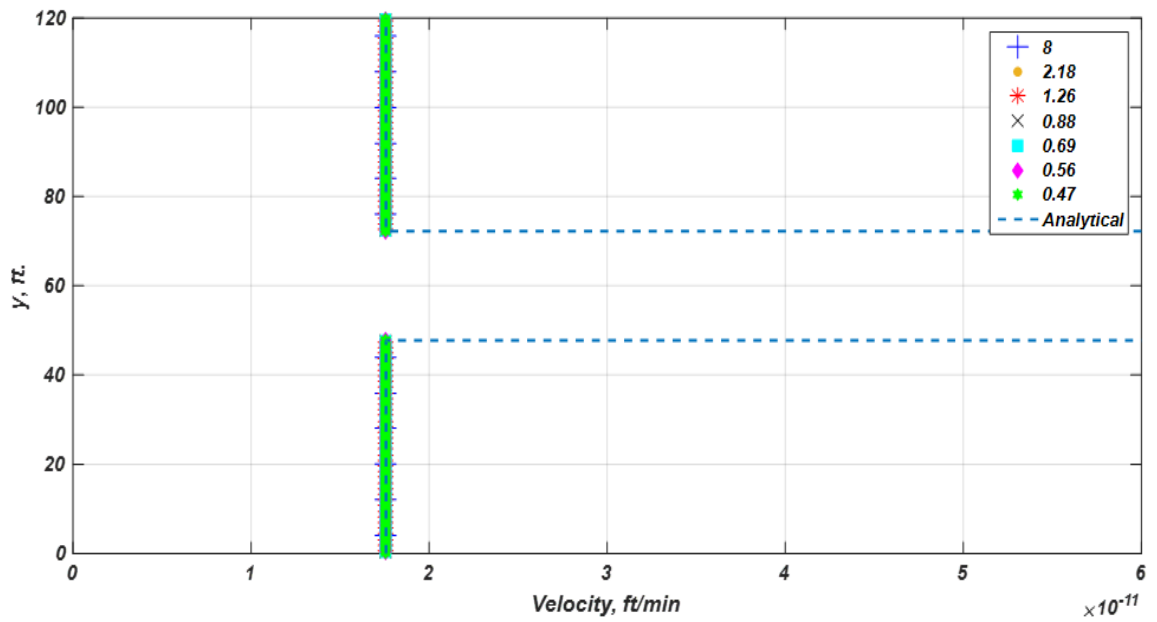


Figure 27 Velocity profile near the interfaces and boundaries using DMEPD at different grid width.

4.2.3. Example 3: Advection-dominant flow in karst reservoir

This example involves the flow of fluid with thermal gradient in a karst reservoir presented previously in Figure 10. The two main differences are that a hot fluid is injected to displace a relatively colder fluid instead of cold fluid displacing hot fluid and two cases involving different fluid properties are considered. In the first case, fluid's viscosity varies slightly with temperature, while in the second case, the fluid's viscosity is a strong function of temperature.

Figure 28 shows the comparison between the heat front generated from the simulation using both Stokes-Brinkman's equation and the DMEPD at 200 *day* for the case in which the viscosity is a weak function of temperature. It is clear that the heat front generated by Stokes-Brinkman's equation is slower than the front generated using the DMEPD. Due to the apparent increase in the area of the free-flow region while using Stokes-Brinkman's equation, the velocity is reduced in the case of constant injection rate. To eliminate the effect of the grid size on the results from the Stokes-Brinkman's model, very fine gridding is used in the free-flow region and the surrounding porous media. The heat front generated from this very fine gridding model is in good match with the results obtained from DMEPD approach as shown in Figure 29.

Stokes-Brinkman's equation takes into consideration the effect of the viscous shear between fluid layers which is mainly controlled by the viscosity, however, DMEPD approach cannot predict the same behavior in the cases that has great change in the viscosity between fluid layers as analytical solution assumes constant fluid viscosity. Figure 30 and Figure 31 show the difference in the produced fluid temperature and the

temperature distribution at using both Stokes-Brinkman's equation and DMEPD approach of a fluid that its viscosity changes sharply with temperature.

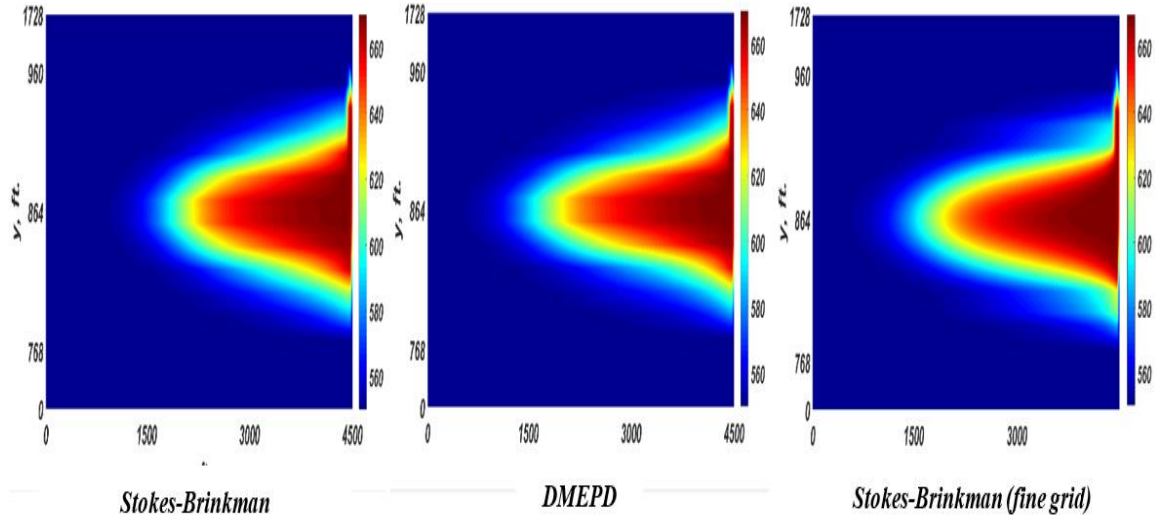


Figure 28 Temperature distribution in $^{\circ}R$ using different approaches at 200 day for constant viscosity fluid (Hint: - the sizes of all the grid blocks are equal for the sake of visualization)

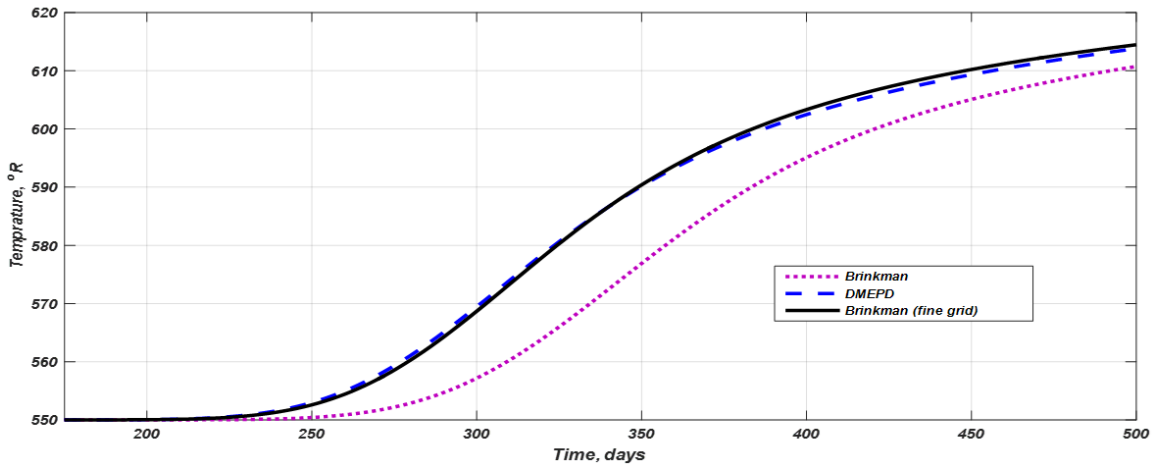


Figure 29 Produced fluid temperature (slight change in viscosity)

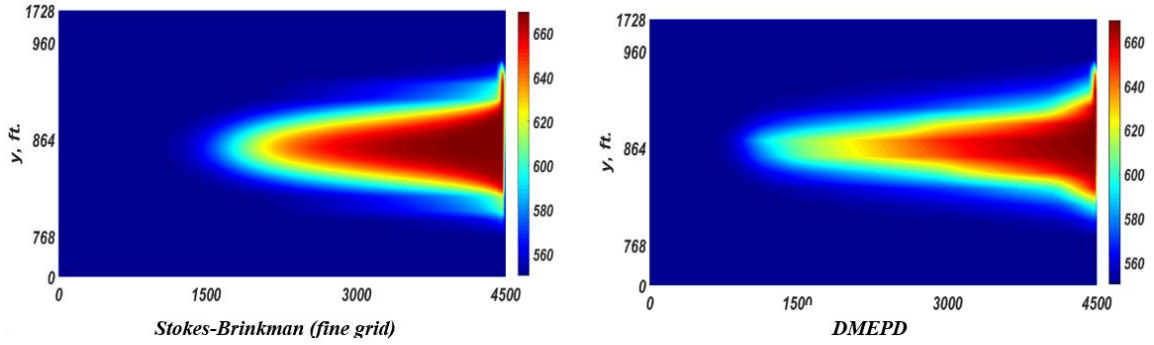


Figure 30 Temperature distribution in °R using different approaches at 200 day for strong variable viscosity fluid (Hint: - the sizes of all the grid blocks are equal for the sake of visualization)

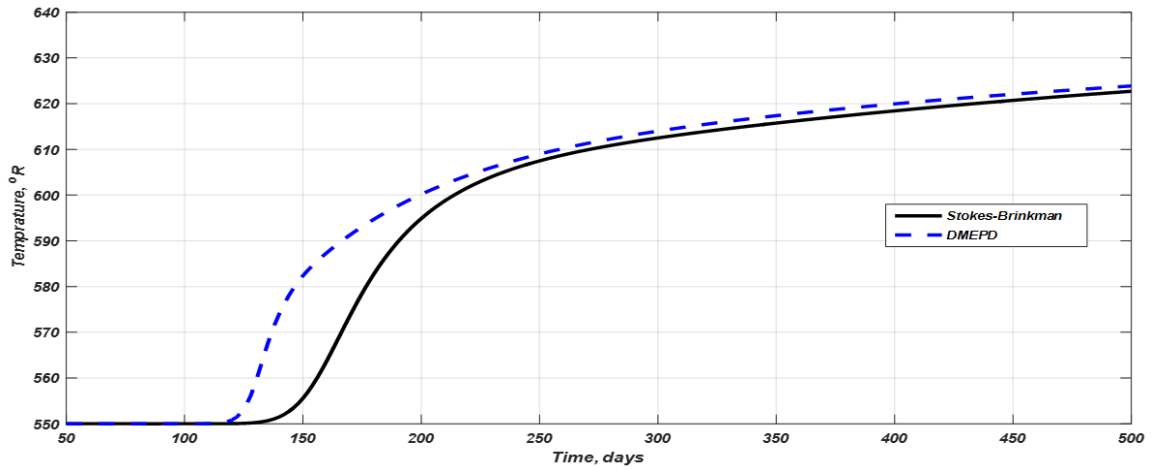


Figure 31 Produced fluid temperature (sharp change in viscosity)

4.2.4. Example 4: Tilted Channel

This case considers the situation when the free-flow region or part of it is not aligned with the selected system axes. Globally coupled pressure method-2 (GCP-2) is implemented to account for the inclination of the free-flow region with selected system directions. The full tensor permeability is calculated using the following relation: -

$$\bar{k} = J \bar{k}_D J^{-1}, \quad (4.3)$$

where $\underline{k}_D = \begin{pmatrix} k_x & 0 \\ 0 & k_y \end{pmatrix}$, $J = \begin{pmatrix} \cos(\theta) & -\sin(\theta) \\ \sin(\theta) & \cos(\theta) \end{pmatrix}$ and θ is the inclination angle of the free-

flow region as shown in Figure 32.

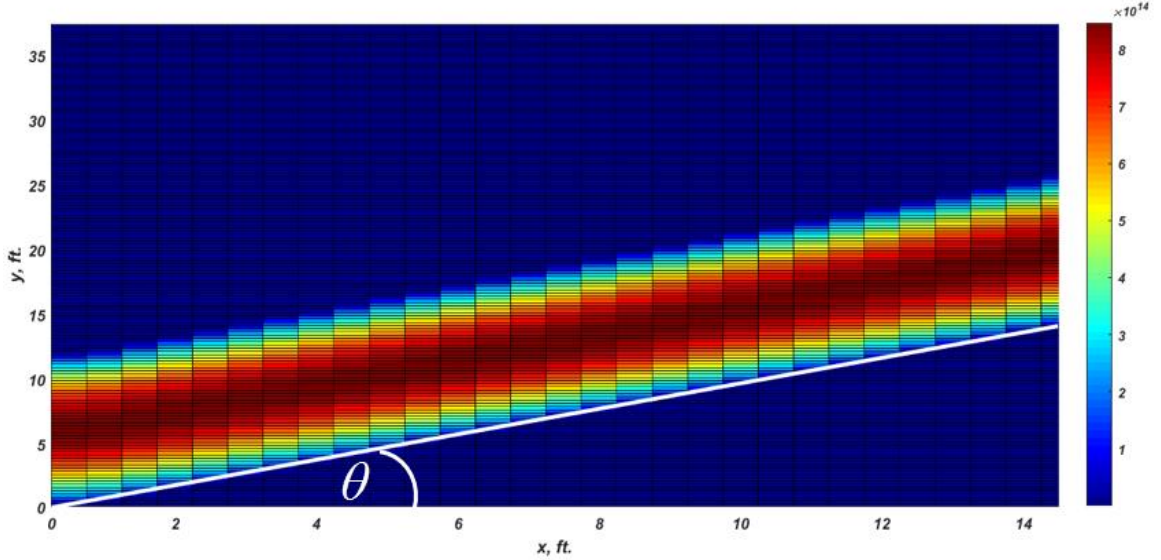


Figure 32 Permeability distribution (md) and inclination angle (θ) of tilted channel case

To investigate the performance comparison between our DMEPD coupled with GCP-2 and Stokes-Brinkman's in the case of tilted channels with non-aligned grids, numerical study is carried on three different inclination angles. The computational domain $[0,15] ft \times [0,37.5] ft$ is meshed by 30×150 cartesian grid. Dirichlet boundary are applied in the x -direction where inlet pressure at left boundary is $1000 psi$ and outlet pressure at right boundary is $500 psi$. The results presented in Figure 33 indicate a match to some degree between two approaches. However, Stokes-Brinkman's approach has difficult time with sharp change in the direction of interfaces in the discrete domain which increases with increasing the inclination angle in our model, DMEPD shows smooth transient in the pressure at the interfaces. Hence, there are some differences in the streamline profile

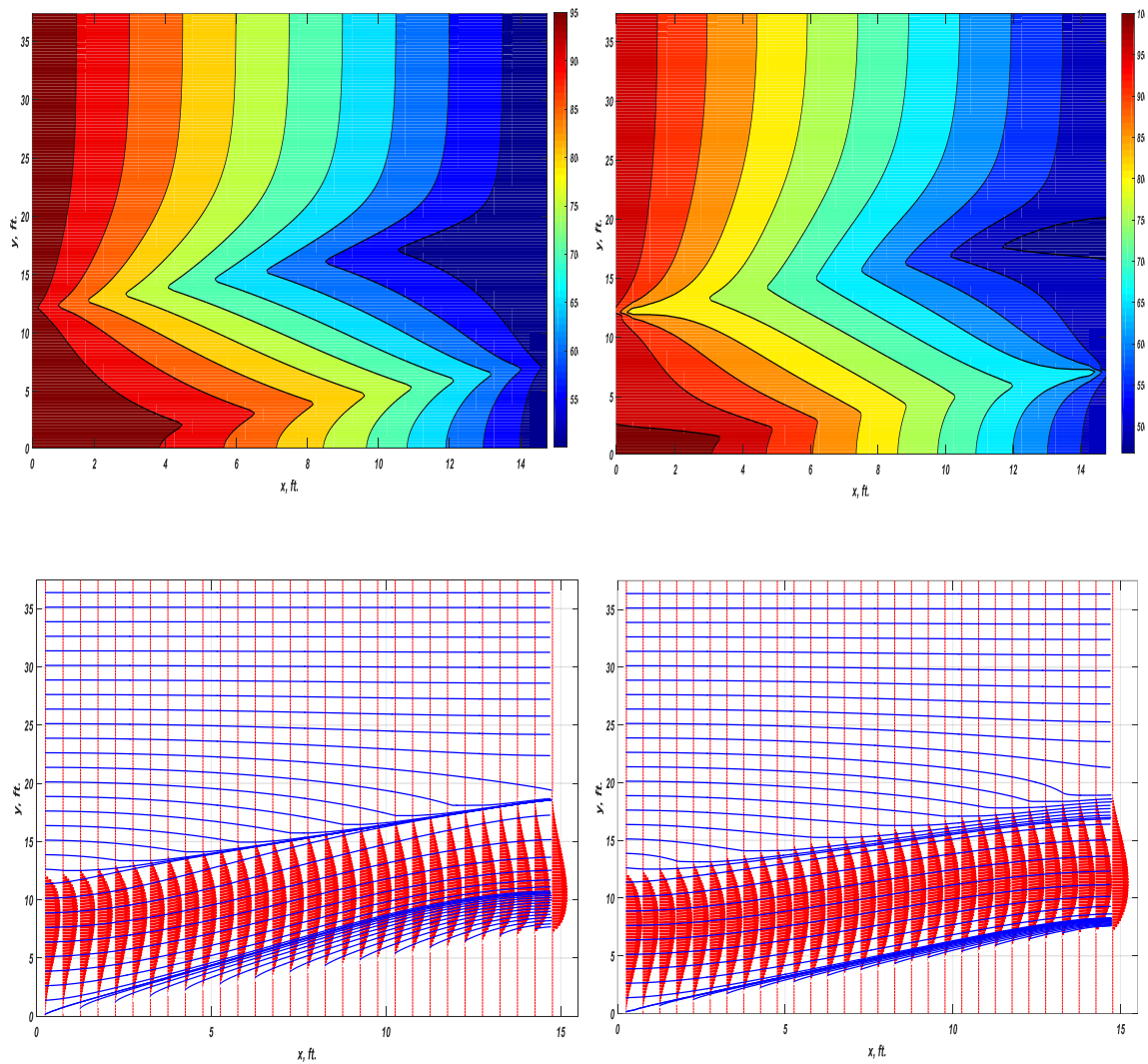
between two methods due to the difference in the pressure around the interfaces. Moreover, it can be noted that Stokes-Brinkman's suffers from monotonicity problem with these sharp interfaces as it is clear from the pressure peaks at location of interfaces in Figure 34. Although, GCP consist of a preprocessing step to form T , the computation cost is still lower than Stokes-Brinkman. For such specific case, the average $\frac{t_{S-B}}{t_{DMEPD}}$ for 100 runs is around 6.718. It worth also to note that, using DMEPD or DMWEPD without considering GCP for the cases that $\theta \neq 0$ nor $\theta \neq \pi/2$ would be fatal mistake as it appears in Figure 35.

4.3. Conclusion

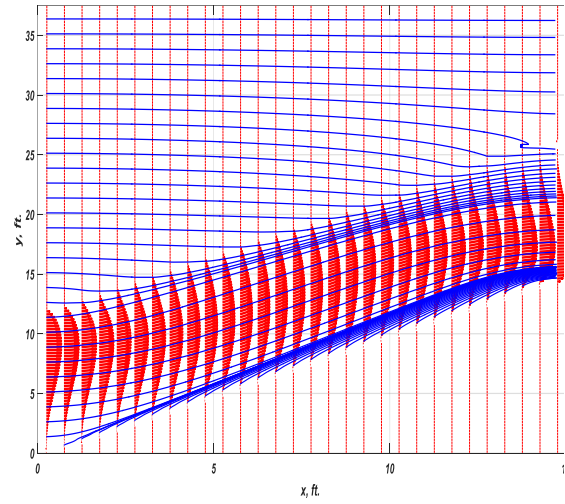
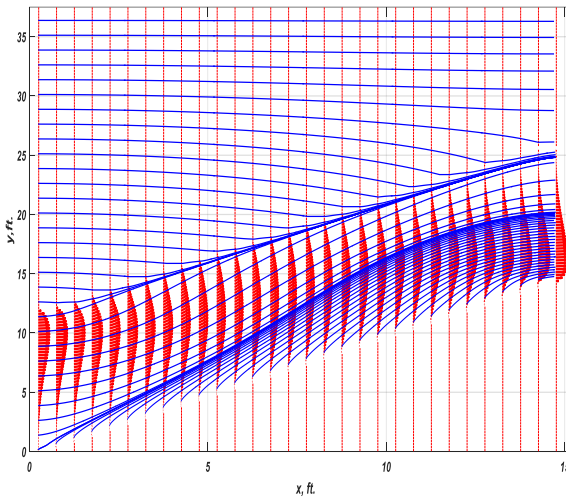
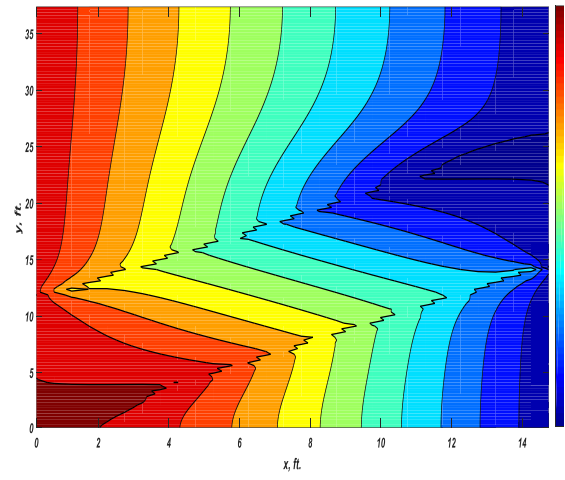
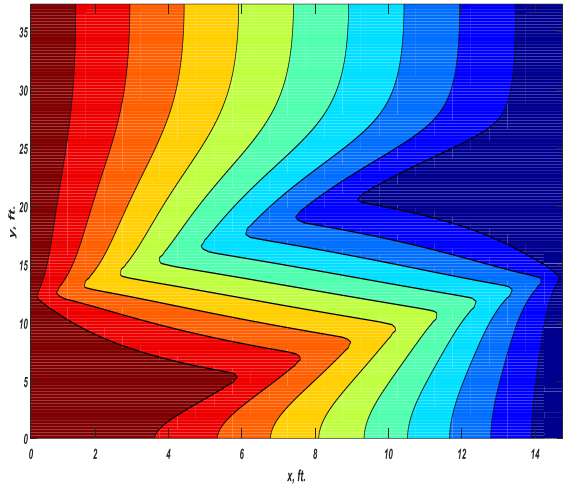
This study demonstrates the importance of Stokes-Brinkman's equation in modeling fluid flow with thermal gradients in of caved aquifers. Stokes-Brinkman's equation can accurately model the actual velocity profile in the free-flow region. In the cases where the advection is dominant, this fluid velocity distribution contributes greatly to the temperature distribution inside the aquifer. Also, the effect of the gridding on the results of the models that utilizes Stokes-Brinkman's equation is significant if large grid cell is used around the interface between the porous media and the free-flow region. The size should be convenient as decreasing the size of the grids under certain limit has negative effect by increasing calculation time and no noticeable impact on the results. Not all the thermal cases that contains free-flow regions are essential to be simulated using Stokes-Brinkman. Only the cases where the advection is dominant are those ones that should be modeled using Stokes-Brinkman.

Another contribution to this study is introducing a new approach called DMEPD approach for simulating karst reservoirs. The apparent permeability inside free-flow region and the

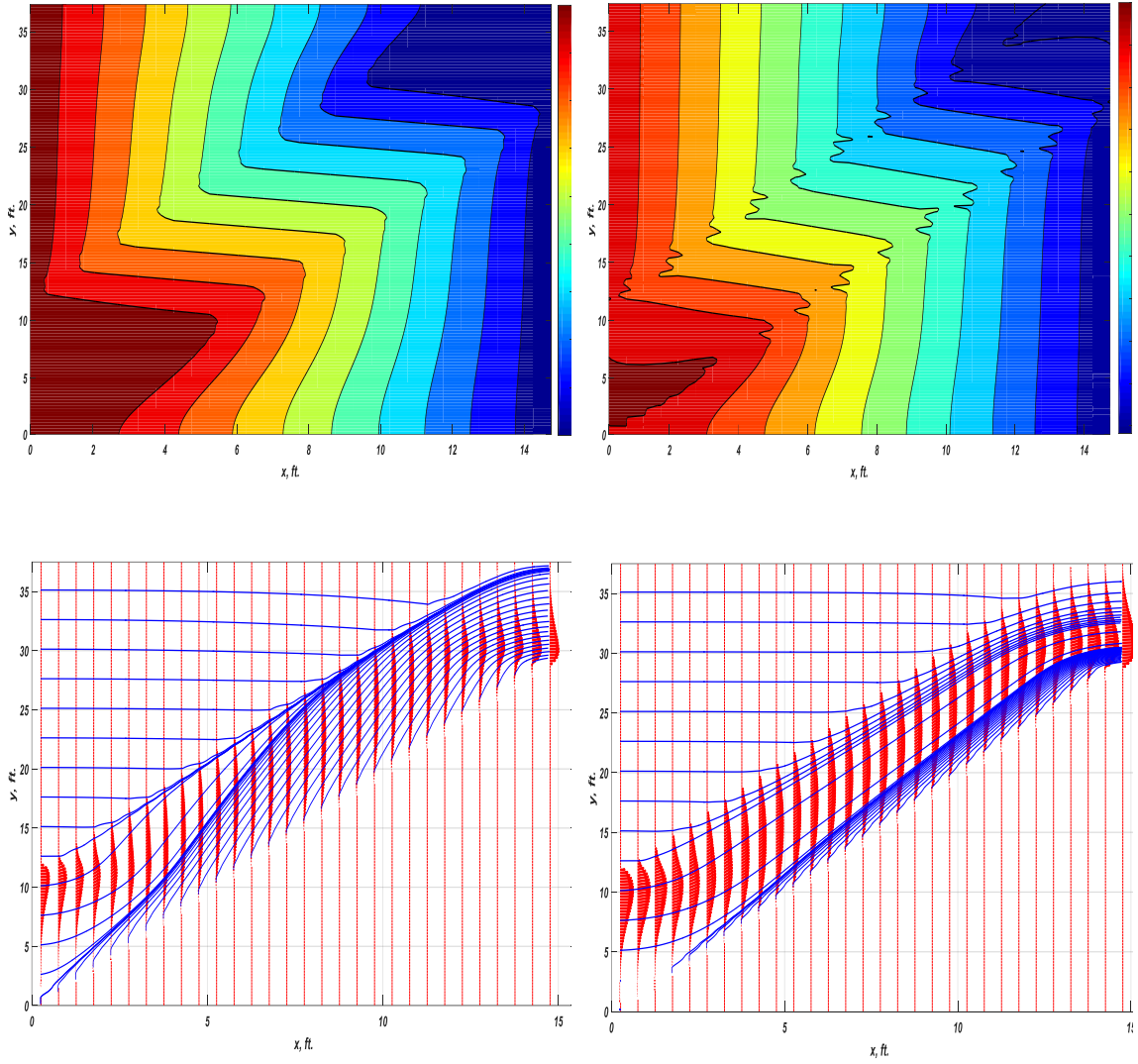
surrounding porous media is calculated from the analytical solution of Stokes-Brinkman's equation. DMEPD can mimic the same behavior predicated by Stokes-Brinkman's equation except for the cases that have sharp change in the fluid viscosity. Also, this approach can be utilized with full tensor permeability to model the cases that consider unalignment of the free-flow region interface with system directions without the need to align the grids with the direction of the channel.



(a) $\theta = \pi/6.776$



(b) $\theta = \pi/4$



$$(c) \theta = \pi/2.838$$

Figure 33 Pressure contour maps (colored maps) and streamline profile (blue) diagram with velocity profile (red) using both DMEPD (left) and Stokes-Brinkman (right) for different inclination angles

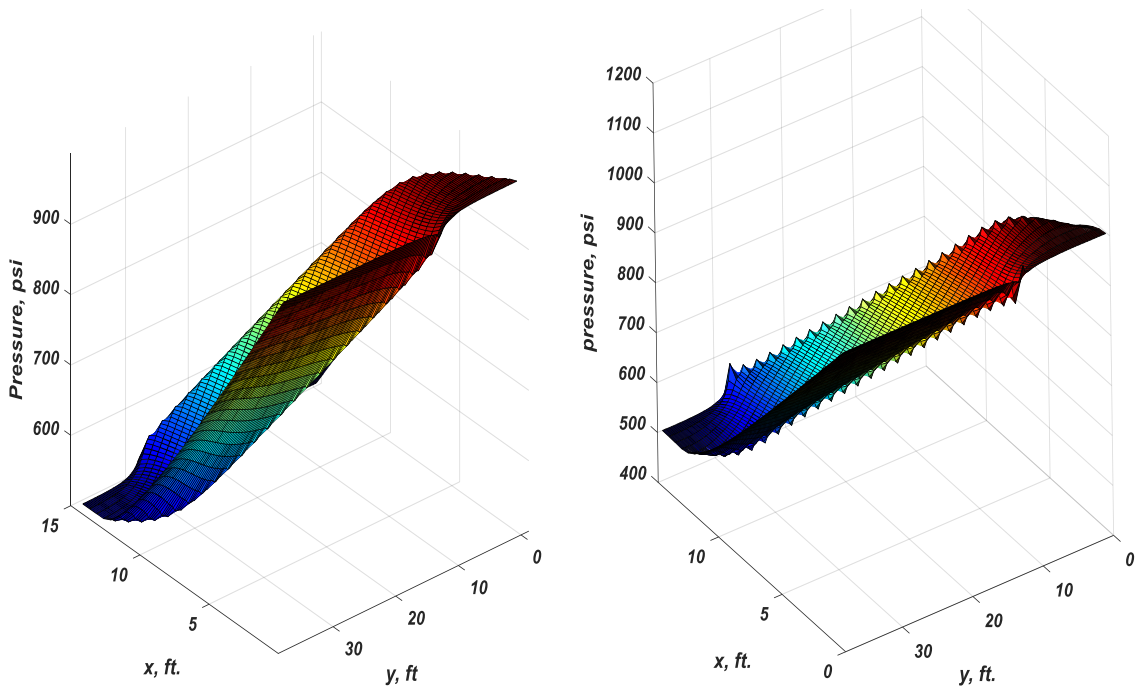


Figure 34 Surface pressure distribution for $\theta = \frac{\pi}{2.838}$ using DMEPD (left) and Stokes-Brinkman (right).

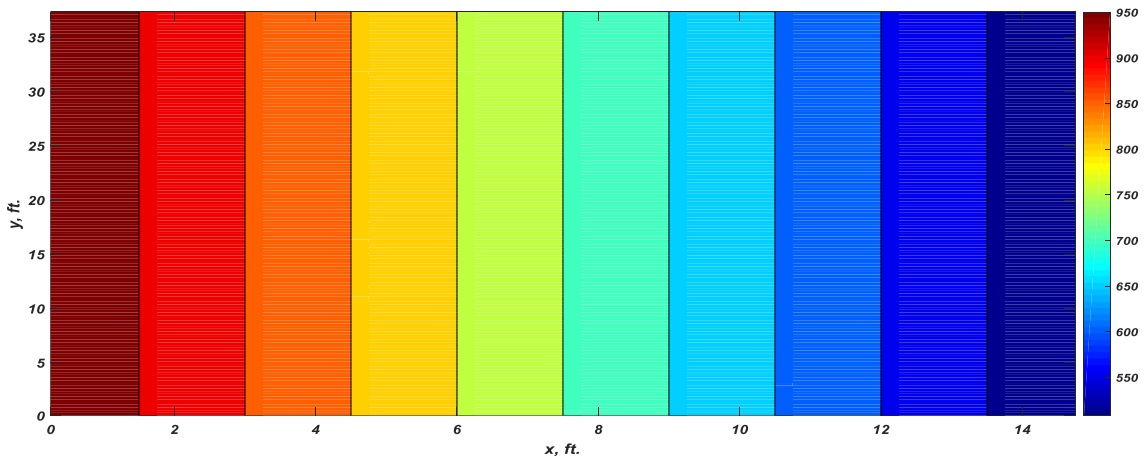


Figure 35 Pressure distribution (psi) using DMWEPD without using GCP

References

- [1] E. Dafny, A. Burg, and H. Gvirtzman, “Effects of Karst and geological structure on groundwater flow: The case of Yarqon-Tananim Aquifer, Israel,” *J. Hydrol.*, vol. 389, no. 3–4, pp. 260–275, Aug. 2010.
- [2] G. Albert, M. Virág, and A. Eröss, “Karst porosity estimations from archive cave surveys - Studies in the Buda Thermal Karst System (Hungary),” *Int. J. Speleol.*, vol. 44, no. 2, pp. 151–165, May 2015.
- [3] J. Chengxin, S. Huapeng, L. Ya, and Y. Hongming, “Numerical simulation of groundwater under complex karst conditions and the prediction of roadway gushing in a coal mine: a case study in the Guang’an Longtan Reservoir in Sichuan Province, China,” *Acta Geochim.*, vol. 35, no. 1, pp. 72–84, Mar. 2016.
- [4] R. Trice, “Challenges And Insights In Optimising Oil Production Form Middle Eastern Karst Reservoirs.,” 2005.
- [5] S. R. Worthington, “A comprehensive strategy for understanding flow in carbonate aquifers,” *Karst Model. Spec. Publ.*, vol. 5, pp. 30–37, 1999.
- [6] Y. V. Dublyansky, “Speleogenetic history of the Hungarian hydrothermal karst,” *Environ. Geol.*, vol. 25, no. 1, pp. 24–35, 1995.
- [7] A. Eröss, J. Mádl-Szőnyi, and A. É. Csoma, “Characteristics of discharge at Rose and Gellért Hills, Budapest, Hungary,” *Cent. Eur. Geol.*, vol. 51, no. 3, pp. 267–281, 2008.
- [8] W. Ufrecht, “Die Stuttgarter Mineralquellen–Geologie und Hydrogeologie im Überblick,” in *Chlorierte Kohlenwasserstoffe im Grundwasser*, Springer, 2015, pp. 5–17.
- [9] J. Corbel, “Karsts du Yucatan et de la Floride,” *Bull. Assoc. Geogr. Fr.*, vol. 36, no. 282, pp. 2–14, 1959.
- [10] S. C. Csallany, “Traité Pratique Des Eaux Souterraines by G. Castany; 661 pages; 125 Francs (\$25.00); Dunod, Paris, France; 1967 (Second Edition).,” *JAWRA J. Am. Water Resour. Assoc.*, vol. 4, no. 1, pp. 81–82, Mar. 1968.
- [11] A. Gulbransen, V. L. Hauge, and K.-A. Lie, “A Multiscale Mixed Finite Element Method for Vuggy and Naturally Fractured Reservoirs,” *SPE J.*, vol. 15, no. 2, pp. 1–4, 2010.
- [12] J. Yao, Z. Huang, Y. Li, C. Wang, X. Lv, and P. Engineering, “SPE 130287 Discrete Fracture-Vug Network Model for Modeling Fluid Flow in Fractured Vuggy Porous Media,” no. 2005, pp. 1–14, 2010.
- [13] G. S. Beavers and D. D. Joseph, “Boundary conditions at a naturally permeable wall,” *J. Fluid Mech.*, vol. 30, no. 1, p. 197, 1967.

- [14] G. S. Beavers, E. M. Sparrow, and R. A. Magnuson, "Experiments on Coupled Parallel Flows in a Channel and a Bounding Porous Medium," *J. Basic Eng.*, vol. 92, no. 4, p. 843, 1970.
- [15] G. Neale and W. Nader, "Practical significance of brinkman's extension of darcy's law: Coupled parallel flows within a channel and a bounding porous medium," *Can. J. Chem. Eng.*, vol. 52, no. 4, pp. 475–478, 1974.
- [16] T. Arbogast, D. S. Brunson, S. L. Bryant, and J. W. Jennings, "A preliminary computational investigation of a macro-model for vuggy porous media," *Dev. Water Sci.*, vol. 55, no. PART 1, pp. 267–278, 2004.
- [17] H. C. Brinkman, "Experimental data on the viscous force exerted by a flowing fluid on a dense swarm of particles," *Appl. Sci. Res.*, vol. 2, no. 1, pp. 155–161, 1949.
- [18] P. Popov, Y. Efendiev, and G. Qin, "Multiscale modeling and simulations of flows in naturally fractured Karst reservoirs," *Commun. Comput. Phys.*, vol. 6, no. 1, pp. 162–184, 2009.
- [19] F. Golfier, D. Lasseux, and M. Quintard, "Investigation of the effective permeability of vuggy or fractured porous media from a Darcy-Brinkman approach," *Comput. Geosci.*, vol. 19, no. 1, pp. 63–78, 2015.
- [20] J. He, J. E. Killough, M. M. Fadlilmula F., and M. Fraim, "Unified Finite Difference Modeling of Transient Flow in Naturally Fractured Carbonate Karst Reservoirs - A 3D Case Study," in *SPE Annual Technical Conference and Exhibition*, 2015.
- [21] J. He, J. E. Killough, M. M. Fadlilmula F., and M. Fraim, "A Unified Finite Difference Model for The Simulation of Transient Flow in Naturally Fractured Carbonate Karst Reservoirs," in *SPE Reservoir Simulation Symposium*, 2015.
- [22] M. Krotkiewski, I. S. Ligaarden, K. A. Lie, and D. W. Schmid, "On the importance of the stokes-brinkman equations for computing effective permeability in karst reservoirs," *Commun. Comput. Phys.*, vol. 10, no. 5, pp. 1315–1332, 2011.
- [23] M. Li *et al.*, "Numerical modeling of geothermal groundwater flow in karst aquifer system in eastern Weibei, Shaanxi Province, China," *Sci. China Ser. D Earth Sci.*, vol. 50, no. S1, pp. 36–41, Jun. 2007.
- [24] P. T. Milanovic, *WATER RESOURCES ENGINEERING in KARST*. Boca Raton, FL: CRC Press, 2004.
- [25] L. Licour, "The geothermal reservoir of Hainaut: the result of thermal convection in a carbonate and sulfate aquifer," *Geol. Belgica*, 2014.
- [26] R. Gauchet and B. Corre, "Rospo Mare field: a unique experience of heavy oil production with horizontal wells in a karst reservoir in presence of a strong tilted hydrodynamics," *Proc. Soc. Pet. Eng. Eur. Pet. Conf.*, p. paper 36869, Jan. 1996.
- [27] G. Bellentani *et al.*, "SPE-181636-MS Rospo Mare Integrated Reservoir Study Italy

, Adriatic Sea: An Innovative Approach of Karst System Modeling and History Match,” in *SPE Annual Technical Conference and Exhibition*, 2016, no. SPE-181636-MS, p. 11.

- [28] F. Fields, *Carbonate Fracture-Cavity Reservoir*. 2013.
- [29] X. Peng, Z. Du, B. Liang, and Z. Qi, “Darcy-Stokes Streamline Simulation for the Tahe-Fractured Reservoir With Cavities,” *SPE J.*, vol. 14, no. September, pp. 543–552, 2009.
- [30] Y. Li, J. Hou, and X. Ma, “Data integration in characterizing a fracture-cavity reservoir, Tahe oilfield, Tarim basin, China,” *Arab. J. Geosci.*, vol. 9, no. 8, Jun. 2016.
- [31] K. K. E. Neuendorf, J. P. M. Jr, and J. A. Jackson, *Glossary of Geology, Fifth Edition*, Fifth edit. American Geosciences Institute, 2011.
- [32] A. D. Howard and C. G. Groves, “Early Development of Karst Systems: 2. Turbulent Flow,” *Water Resour. Res.*, vol. 31, no. 1, pp. 19–26, Jan. 1995.
- [33] L. Kiraly, “Rapport sur l’état actuel des connaissances dans le domaine des caractères physiques des roches karstiques,” in *Hydrogeology of Karstic Terrains*, no. 3, 1975, pp. 53–67.
- [34] D. C. Ford, “Perspectives in karst hydrogeology and cavern genesis,” *Karst Model.*, no. 1903, p. 12, 1999.
- [35] S. R. H. Worthington, D. C. Ford, and P. A. Beddows, “Porosity and permeability enhancement in unconfined carbonate aquifers as a result of solution,” in *Speleogenesis: Evolution of Karst Aquifers*, 2000, pp. 427–463.
- [36] A. B. Klimchouk and D. C. Ford, “Types of karst and evolution of hydrogeologic settings,” *Speleogenes. Evol. karst aquifers*, no. MAY, pp. 45–53, 2000.
- [37] M. Filipponi, P. Y. Jeannin, and L. Tacher, “Evidence of inception horizons in karst conduit networks,” *Geomorphology*, vol. 106, no. 1–2, pp. 86–99, 2009.
- [38] C. Zou and C. Zou, “Chapter 6 – Carbonate Fracture-Cavity Reservoir,” in *Unconventional Petroleum Geology*, 2013, pp. 191–221.
- [39] N. Goldscheider, J. Mádl-Szőnyi, A. Eröss, and E. Schill, “Review: Thermal water resources in carbonate rock aquifers,” *Hydrogeol. J.*, vol. 18, no. 6, pp. 1303–1318, Sep. 2010.
- [40] Z. Chen, *Reservoir simulation: mathematical techniques in oil recovery*. Philadelphia, PA: SIAM/Society for Industrial and Applied Mathematics, 2007.
- [41] H. Darcy, *Les fontaines publiques de la ville de Dijon: exposition et application...* 1856.
- [42] M. Sahraoui and M. Kaviany, “Slip and no-slip velocity boundary conditions

interface of porous media,” *Mech. Eng.*, vol. 35, no. 4, pp. 927–943, Apr. 1992.

- [43] A. Marciniak-Czochra and A. Mikelić, “Effective Pressure Interface Law for Transport Phenomena between an Unconfined Fluid and a Porous Medium Using Homogenization,” *Multiscale Model. Simul.*, vol. 10, no. 2, pp. 285–305, Jan. 2012.
- [44] J. Koplik, “Viscosity renormalization in the Brinkman equation,” *Phys. Fluids*, vol. 26, no. 10, p. 2864, 1983.
- [45] C. G. Aguilar-Madera, F. J. Valdés-Parada, B. Goyeau, and J. A. Ochoa-Tapia, “Convective heat transfer in a channel partially filled with a porous medium,” *Int. J. Therm. Sci.*, vol. 50, no. 8, pp. 1355–1368, Aug. 2011.
- [46] Y. Mahmoudi and M. Maerefat, “Analytical investigation of heat transfer enhancement in a channel partially filled with a porous material under local thermal non-equilibrium condition,” *Int. J. Therm. Sci.*, vol. 50, no. 12, pp. 2386–2401, Dec. 2011.
- [47] L. Durlofsky and J. F. Brady, “Analysis of the Brinkman equation as a model for flow in porous media,” *Phys. Fluids*, vol. 30, no. 11, p. 3329, 1987.
- [48] P. M. Adler and P. M. Mills, “Motion and Rupture of a Porous Sphere in a Linear Flow Field,” *J. Rheol. (N. Y. N. Y.)*, vol. 23, no. 1, pp. 25–37, Feb. 1979.
- [49] S. Kim and W. B. Russel, “Modelling of porous media by renormalization of the Stokes equations,” *J. Fluid Mech.*, vol. 154, no. 1, p. 269, May 2006.
- [50] D. A. Nield and A. Bejan, *Convection in porous media*, vol. 24. 2013.
- [51] H. A. Belhaj, K. R. Agha, S. D. Butt, and M. R. Islam, “A Comprehensive Numerical Simulation Model for Non-Darcy Flow including Viscous, Inertial and Convective Contributions,” 2003.
- [52] I. Aavatsmark, T. Barkve, O. Bøe, and T. Mannseth, “Discretization on Unstructured Grids for Inhomogeneous, Anisotropic Media. Part I: Derivation of the Methods,” *SIAM J. Sci. Comput.*, vol. 19, no. 5, pp. 1700–1716, Sep. 1998.
- [53] I. Aavatsmark, T. Barkve, O. Bøe, and T. Mannseth, “Discretization on Unstructured Grids For Inhomogeneous, Anisotropic Media. Part II: Discussion And Numerical Results,” *SIAM J. Sci. Comput.*, vol. 19, no. 5, pp. 1717–1736, Sep. 1998.
- [54] I. Aavatsmark, “An Introduction to Multipoint Flux Approximations for Quadrilateral Grids,” *Comput. Geosci.*, vol. 6, no. 3/4, pp. 405–432, 2002.
- [55] I. Aavatsmark, G. T. Eigestad, B. T. Mallison, and J. M. Nordbotten, “A compact multipoint flux approximation method with improved robustness,” *Numer. Methods Partial Differ. Equ.*, vol. 24, no. 5, pp. 1329–1360, Sep. 2008.
- [56] J. M. Nordbotten and G. T. Eigestad, “Discretization on quadrilateral grids with

improved monotonicity properties,” *J. Comput. Phys.*, vol. 203, no. 2, pp. 744–760, Mar. 2005.

- [57] Q. Y. Chen, J. Wan, Y. Yang, and R. T. Mifflin, “Enriched multi-point flux approximation for general grids,” *J. Comput. Phys.*, vol. 227, no. 3, pp. 1701–1721, Jan. 2008.
- [58] W. Zhang and M. Al Kobaisi, “A Globally Coupled Pressure Method for the Discretization of the Tensor-Pressure Equation on Non-K-orthogonal Grids,” *SPE J.*, vol. 22, no. 2, pp. 679–698, Apr. 2017.
- [59] J. F. Douglas, J. M. Gasiorek, J. a. Swaffield, and L. B. Jack, *FLUID MECHANICS*, Fifth Edit. Pearson/Prentice Hall, 2012.

|

Appendix : Analytical solution of Stokes-Brinkman's Equation

If we neglect the body force, Equation (2.7) can be written for flow in only x-direction as:

-

$$\frac{\mu}{k_x} u_x = -\frac{\partial p}{\partial x} + \mu^* \frac{\partial^2 u_x}{\partial y^2}. \quad (\text{A.1})$$

Equation (A.1) has two components: one in the free-flow region and the other in the porous media. The component in the free-flow region is given by: -

$$0 = -\frac{\partial p}{\partial x} + \mu \frac{\partial^2 v_x}{\partial y^2} \quad (\text{A.2})$$

and the one in the porous media given by: -

$$\frac{\mu}{k_x} u_x = -\frac{\partial p}{\partial x} + \mu^* \frac{\partial^2 u_x}{\partial y^2}. \quad (\text{A.3})$$

Because $\partial p/\partial x$ is constant throughout the entire domain, Equations (A.2) and (A.3) are ordinary differential equations in y with unknowns v_x and u_x , respectively. To solve this problem, we assume a single-phase fluid, an incompressible system and that the pressure gradient is constant and the same in both the porous media and the free-flow region. Also, the Reynolds number is small such that the flow under the consideration is laminar [59]. The flow is fully developed in the x -direction. The following physical conditions are used:

-

- Inside the free-flow region ($0 < y < w$), $k_x \rightarrow \infty$ and $\mu^* = \mu$

- In Porous Media 1 ($y > w$) (see Figure 4) $\mu^* = \mu_1^*$ and $k_x = k_1$. While in Porous Media 2 ($y < 0$), $\mu^* = \mu_2^*$ and $k_x = k_2$.

Also, the continuity of the actual velocity and that of its derivative at the interfaces between the free-flow region and the two-porous media are enforced by the four interface conditions.

- Interface between the free-flow region and Porous Media 1 ($y = w$)

1. The continuity of the actual velocity is given by: -

$$\mu v_x = \mu_1^* u_x. \quad (\text{A.4})$$

2. The continuity of its derivative is expressed as: -

$$\mu \frac{dv_x}{dy} = \mu_1^* \frac{du_x}{dy}. \quad (\text{A.5})$$

- Interface between the free-flow region and Porous Media 2 ($y = 0$)

3. The continuity of the actual velocity is given by: -

$$\mu v_x = \mu_2^* u_x. \quad (\text{A.6})$$

4. The continuity of its derivative is expressed as: -

$$\mu \frac{dv_x}{dy} = \mu_2^* \frac{du_x}{dy}. \quad (\text{A.7})$$

The solutions to Equations (A.2) and (A.3) are straightforward and are obtained by integrating with respect to y twice. Thus, we obtain: -

$$v_x = \frac{1}{\mu} (0.5 \frac{\partial p}{\partial x} y^2 + c_1 y + c_2), \quad (\text{A.8})$$

as the solution to Equation (A.2) and

$$u_x = c e^{-\lambda y} - \frac{k_x}{\mu} \frac{\partial p}{\partial x}, \quad (\text{A.9})$$

as the solution to Equation (A.3). Note that c_1, c_2 and c in Equations (A.8) and (A.9) are the coefficients of integration. The solution in Equation (A.8) is valid in the free-flow region ($0 < y < w$) while that in Equation (A.9) is valid in the porous media. However, because we have two porous media separated by the free-flow region, Equation (A.9) should be written for the two-porous media as: -

$$u_{x_1} = c_3 e^{-\lambda_1 y} - \frac{k_1}{\mu} \frac{\partial p}{\partial x} \quad (\text{A.11})$$

for Porous Media 1 ($y > w$) and

$$u_{x_2} = c_4 e^{\lambda_2 y} - \frac{k_2}{\mu} \frac{\partial p}{\partial x} \quad (\text{A.12})$$

In Equations (A.10) and (A.11), $\lambda_1 = \sqrt{\frac{\mu}{\mu_1^* k_1}}$ and $\lambda_2 = \sqrt{\frac{\mu}{\mu_2^* k_2}}$. We see from the solutions in (A.9) and (A.10), that as $y \rightarrow \infty$ in (A.9) and $y \rightarrow -\infty$ in (A.10), the velocity u_x tends towards Darcy's law as the first term on the right-hand-side in each of these equations tends to zero. That means that as we move deeper into the porous media the effect of the free-flow region on the flow within the porous media becomes negligible. The coefficients

and in Equations. (A.8-A.11) can be obtained by applying the interface conditions in (A.4-A.7) to obtain: -

$$c_1 = \frac{-\frac{\partial p}{\partial x}}{\left(1 + \lambda_2 w + \frac{\lambda_1}{\lambda_2}\right)} \left(w \left(1 + \frac{\lambda_2 w}{2}\right) + \frac{\lambda_2 (\mu_2^* k_2 - \mu_1^* k_1)}{\mu} \right),$$

$$c_2 = \frac{-\partial p / \partial x}{\lambda_3 \left(1 + \lambda_2 w + \frac{\lambda_1}{\lambda_2}\right)} \left(w \left(1 + \frac{\lambda_2 w}{2}\right) + \frac{\lambda_2 (\mu_2^* k_2 - \mu_1^* k_1)}{\mu} \right) - \frac{\mu_1^* k_1}{\mu} \frac{\partial p}{\partial x},$$

$$c_3 = \frac{e^{\lambda_2 w}}{\mu_2^*} \left(\frac{w^2}{2} - \frac{\mu_1^* k_1}{\mu} \right) \frac{\partial p}{\partial x} + e^{\lambda_2 w} \frac{k_2}{\mu} \frac{\partial p}{\partial x} + \frac{e^{\lambda_2 h}}{\mu_2^*} \left(w + \frac{1}{\lambda_1} \right) c_1,$$

and

$$c_4 = \frac{-\partial p / \partial x}{\mu_1^* \lambda_1 \left(1 + \lambda_2 w + \frac{\lambda_1}{\lambda_2}\right)} \left(w \left(1 + \frac{\lambda_2 w}{2}\right) + \frac{\lambda_2 (\mu_2^* k_2 - \mu_1^* k_1)}{\mu} \right),$$

We can then determine the location of maximum flow velocity in the free-flow region by enforcing the first order optimality condition ($\partial v_x / \partial y = 0$) to obtain: -

$$y_{v_{\max}} = \frac{1}{\left(1 + \lambda_2 w + \frac{\lambda_1}{\lambda_2}\right)} \left(w \left(1 + \frac{\lambda_2 w}{2}\right) + \frac{\lambda_2 (\mu_2^* k_2 - \mu_1^* k_1)}{\mu} \right) \quad (\text{A.13})$$

Vitae

Name :AbdAllah AbdRabElNaby Youssef ElSaieed |

Nationality :Egypt |

Date of Birth :3/10/1991|

Email :abdallah_youssef@ymail.com|

Address :El-Kom El-Taweel, Biela, Kafr ElShyiekh, Egypt|

Academic Background :Bachelor of Petroleum Engineering from Suez University
in May 2013 |